Primacy of vision shapes behavioral strategies and neural substrates of spatial navigation in the hippocampus of the common marmoset

Authors:

Diego B. Piza[1], Benjamin W. Corrigan[1], Roberto A. Gulli[3], Sonia Do Carmo[5], A. Claudio Cuello[5], Lyle Muller[4], Julio Martinez-Trujillo[1,2]

Affiliations:

1. Schulich School of Medicine and Dentistry, London, ON, Canada.
2. Western University, Departments of Physiology and Pharmacology, and Psychiatry.
3. Zuckerman Institute, Columbia University.
4. Department of Applied Mathematics, Western University, Ontario, Canada.
5. McGill University, Department of Pharmacology and Therapeutics, Montreal, QC, Canada.

Abstract:

The mammalian hippocampus has been compared to a Global Positioning System (GPS) that enables spatial navigation. This notion has been primarily drawn from studies conducted in nocturnal mammals, such as rats; that lack many adaptations to daylight vision compared to diurnal primates. Here we demonstrate that during foraging in a 3D maze, the common marmoset, a new world diurnal primate with foveal, stereo-color vision, predominantly uses rapid head-gaze shifts to visually explore their surroundings while remaining stationary, and then minimizes head movements to navigate towards goals. On the other hand, rats, mainly move their head at low velocities while locomoting to explore the environment using their whiskers. These differences in exploration-navigation strategies reflect the species' sensory adaptations to different ecological niches. In the marmoset hippocampus CA3/CA1 regions putative pyramidal neurons show selectivity for 3D view, head direction, and less for place, but mainly mixed selectivity for combinations of these variables. Despite weak place selectivity, the spatial position of the animal in the maze can be decoded from the activity of small ensembles of mixed selective neurons. Inhibitory interneurons are tuned to 3D angular head velocity and translation speed, with most cells showing mixed selectivity for both variables. Finally, marmosets lack the rhythmic theta oscillations of local field potentials seen during locomotion in rats. Instead, they show resetting of theta oscillations triggered by head-gaze shifts that co-occurred with the activation of inhibitory interneurons, followed by various modulations in the activity of pyramidal cells. Our results show that the marmoset visual exploration/navigation strategies and the hippocampal neuronal specializations supporting them diverge from those observed in rats, reflecting the far-sensing capabilities of the marmoset visual system adapted to diurnal lifestyle.

Introduction:

The hippocampus is a phylogenetically ancient structure of the mammalian brain that has been implicated in spatial memory and navigation[1–3]. Understanding how the hippocampus supports a

cognitive map-like representation of the outer world first came from recordings of single-neuron spiking activity in freely moving rats, describing individual neurons that selectively increased their firing rate when subjects occupied a specific location within a maze[1,4]. Following the discovery of place cells, a rich diversity of spatial encoding neurons has been reported within the hippocampal formation and in functionally related brain areas[5–13]. Based on the results of spatial navigation studies in rodents, the hippocampus has been deemed a Global Positioning System (GPS) that enables the formation of a cognitive map of the environment. However, recent navigation studies in primate species such as macaques and marmosets have not replicated the range of neuronal selectivities found in the hippocampus of rats and mice[14,15]. Thus, it is unclear whether the analogy of the hippocampus as a GPS generalizes to the aforementioned primate species.

In primates, hippocampus studies are much scarcer than in rats and mice. Some studies in macaque monkeys have reported that neurons in the hippocampus encode the direction of the subject's gaze in space (view)[14,16–20]. It has been proposed that diurnal primates' highly developed visual capabilities[21] may have shaped neuronal selectivities in the hippocampus[18,22,23]. Indeed, macaques and marmosets with diurnal lifestyle and foveal, stereoscopic color vision, have developed a head-gaze control system that allows orienting the fovea towards locations of interest while inspecting visual scenes[24–26]. However, several studies in non-human primates (NHPs) have mainly used paradigms in which the subject is placed in a primate chair with the head and/or body restrained while performing visual tasks on a computer screen[27–29]. These experimental paradigms may deprive the hippocampus of multisensory inputs such as vestibular and proprioceptive that occur during real-world navigation.

A few studies in freely moving monkeys[14,30–32] have reported that some hippocampal neurons are tuned for variables related to place, gaze direction or view, head movements and the interaction between view and place. One study trained marmosets to navigate a linear maze under constrained conditions (tethered) and described the existence of place-like cells in the hippocampus[15]. Interestingly, they describe that rhythmic hippocampal theta oscillations are not omnipresent during locomotion-exploratory behavior[15], as is the case in mice and rats[3,33]. In other mammalian species, such as the Egyptian fruit bat[34] theta oscillations in the hippocampus occur in short bouts. Finally, some studies have documented that in humans and macaque monkeys, theta oscillations are coupled to saccades, and they have variable frequencies[35–37].

In the present study, we test the hypothesis that diurnal primates have developed different exploration-navigation strategies compared to nocturnal rodents such as rats, and that such strategies have shaped the physiology of the hippocampus. We investigate the exploration-navigation strategies of marmosets during unrestricted 3D foraging and compare them to those of freely moving rats. We built a setup that allowed for continuous tracking of the marmoset body position and head direction in 3D and recording neural activity from the hippocampus (CA3 and CA1) wirelessly. We found that marmosets navigate 3D environments using quadrupedal locomotion, during which the head-gaze remains relatively stable. They make frequent stops, during which they execute sequences of rapid head-gaze movements toward locations of interest (visual exploration). This is different from rats that often move their heads at low velocities during locomotion, 'scanning' the environment with their whiskers[38]. Additionally, we use wireless recordings of neural activity and demonstrate that marmoset hippocampal neurons in subfields

CA3 and CA1 predominantly encode a mix of variables related to 3D head/gaze direction, speed, and position in space. We found a predominance of 3D view, head direction and spatial position coding in putative pyramidal (principal) cells, and a mix of 3D angular head velocity (AHV) and translation speed (TS) in putative interneurons. We demonstrate that from small ensembles of mixed selective neurons, weakly tuned for spatial position, we could reliably decode the subject's position in the maze. Finally, we demonstrated that rapid head-gaze movements reset local field potentials (LFP) theta oscillations in the hippocampus, which coincides with an increase in the response of interneurons followed by modulation of pyramidal neurons' firing.

Results

Spatial exploration strategies in marmosets and rats

We measured position and head direction signals in two freely moving marmosets (1 male and 1 female) while they foraged through a 3D maze searching for reward (e.g., condensed milkshake or marshmallows; **Fig. 1a**, **Fig. S1g**, methods). A reward was delivered at 1 of the 12 possible maze locations randomly selected (**Fig. 3b**), by either cueing the subject with an LED light or waving a hand at the reward location; this reward schedule was used to encourage navigation of the 3D maze. Recorded data consisted of 6 different variables, three for the position of the subject in the maze (horizontal or Xp, depth or Yp, vertical or Zp), and 3 for rotational head direction (Xh, Yh, Zh) yaw, roll and pitch. Body position signals were low-pass filtered at 4Hz. TS was calculated from the position signals (see methods).

Xh, Yh, and Zh rotation vectors were used to calculate the AHV (see methods). We then classified rapid translation or rapid head rotation movements based on a minimum speed/velocity threshold (higher than 15cm/s TS and 200°/s AHV, for body translation and head rotation movements respectively) and amplitude threshold (30cm and 16° for body translation and head rotation movements respectively).

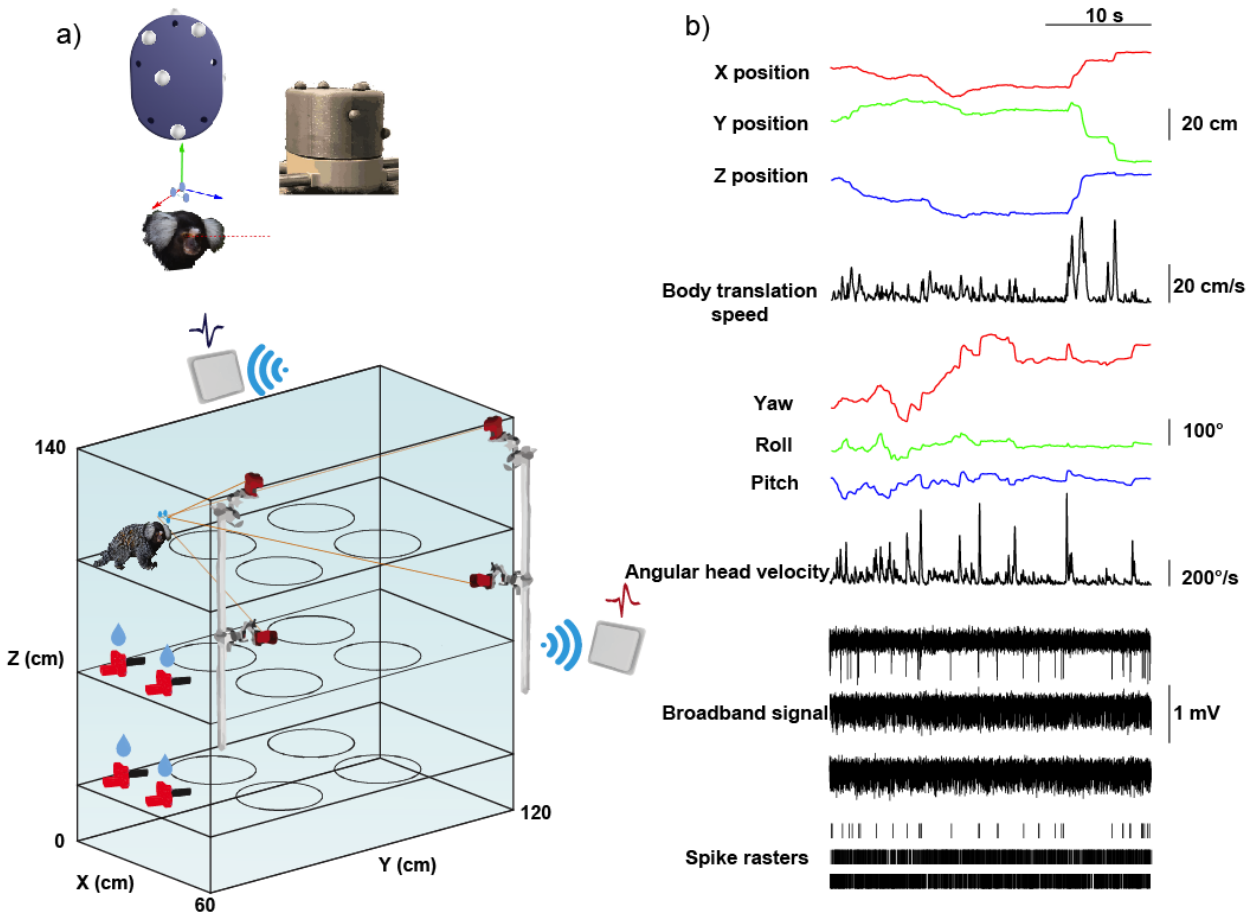

Figure 1 | Behavioral setup and data traces. (**a**) Top, recording chamber cap cover with a schematic of marker positions that allow tracking position and direction of the subject's head. Bottom, a schematic of the maze and wireless recording setup. (**b**) Data traces with three example single cells. The type of signal and corresponding units are indicated. In the spike rasters, each vertical line indicates an action potential.

We observed that during foraging marmosets alternate between periods in which the subjects translate in 3D space (quadrupedal locomotion) while the head remains 'fixed' relative to the body, and periods in which they stop translating in space (body stationary), and the head frequently rotates relative to the body (supplementary movie 1). During the latter periods, they explore the environment through frequent rapid head movements that end in gaze fixations[39], resembling the way humans and other primates freely explore visual scenes[25]. We will refer to these rapid head movements as head-gaze shifts since the main goal is to align the gaze with objects/locations of interest. To corroborate this observation, we computed translation trajectories and associated velocities. Indeed, marmosets alternated between translations during which head-gaze movements were scarce (**Fig. 2a**, left, blue trajectories) and stops during which head movements were frequent (**Fig. 2a**, left, red dots).

To contrast the navigation strategies of marmosets and rats, we performed the same analyses in a dataset available online (CRCNS.org, Data sharing, hc-2 data set) collected while rats were

foraging in a maze searching for rewards. Rats were video-tracked (sampled at 39.06Hz) using two LEDs of different colors, placed on the front and back of the head, from which the position and head direction can be measured[40]. Rats are nocturnal; their vision has adapted to detect motion in dim light conditions. Their retinas possess ultraviolet-sensitive cones, and the majority of their optic nerve axons target the superior colliculus (SC) rather than the lateral geniculate nucleus (LGN)[41]. Although rats possess visual capabilities and can perform visual tasks[42], they have no well-defined fovea, their spectral sensitivity is considerably smaller than that of diurnal primates, and the anatomical position of their eyes does not enable stereo vision to the same degree as front-positioned eyes primates[41,43]. Consequently, rats must rely to a larger degree on olfaction and whisking to sense the environment. Most of the rat's eye movements are often disconjugated[44] and stabilize the eyes against movements of the head.

We found that rats' head movements often occurred simultaneously with the body translation movements during locomotion (**Fig. 2a**, right, green dots). In marmosets, 80% (99% confidence interval [79%, 80%]) of the head movements occurred during body stops while in the rat only 14% (99%, confidence interval [12%, 14%]) of the head movements occurred during body stops (**Fig. 2b**, left pie chart). On the other hand, in marmosets, only 20% (99% confidence interval [19%, 20%]) of the head movements occurred during body translations while in rats 86% (99% confidence interval [85%, 87%]) of the head movements occurred during translations (**Fig. 2b**, right pie chart). The range of TS and AHV in the marmoset appears larger than in the rat which may reflect different adaptations in the two species. The AHV in the marmoset has a long tail along the X-axis corresponding to low TS compared to the rat (**Fig. 2b**). This is due to the high frequency of rapid head-gaze movements in the marmoset when the body is stationary.

Rapid head-gaze movements in the marmoset have the signature of gaze shifts composed of coordinated movements of the eyes and the head. The main sequence, described as the relationship between the amplitude and peak velocity of eye saccades has been used to characterize gaze shifts[45]. During gaze shifts the peak velocity/speed increases monotonically with increases in head movement or saccade amplitude, progressively saturating for large movements[25]. Marmoset rapid head movements, much like eye movements, are stereotyped ballistic movements used for visual exploration; and the main sequence has been used to describe their kinematics[39]. We hypothesize that in the marmoset the main sequence of the head movements will follow a similar profile as the main sequence of gaze shifts in macaques. On the other hand, rats, lacking a sophisticated head-gaze apparatus would systematically show lower peak velocities relative to marmosets.

To test this hypothesis, we computed the main sequence of head movements (movement amplitude vs. peak velocity) in both species. In both, marmosets and rats head peak velocity increased as a function of movement amplitude (**Fig. 2c**) indicating a general kinematic principle also reported in other species[46]. Importantly, head movements of the same amplitude have higher mean peak velocity in the marmoset than in the rat (two-sided Wilcoxon signed-rank test, $p < 5 \times 10^{-324}$, Z=113.8). The maximum response (Rmax) of a Naka-Rushton function fit to the velocity as a function of movement amplitude is higher for marmosets compared to rats (795°/s vs 430.9°/s; **Fig. 2c, Fig. S1 c,d**). These results are consistent with marmosets' use of head-gaze shifts to visually explore the environment during body stops to position and stabilize the fovea on objects of interest. On the other hand, rats use head scanning mainly during locomotion to orient the

whiskers and facilitate exploration[47,48]. Rats may also use vision but with their lack of fovea and poor color and stereo vision, they may not require image stabilization to the same degree as marmosets do[44,49].

We did not measure eye position in the marmosets in the 3D maze, but instead relied on head movements as a proxy for gaze direction, thus marmosets may have moved the eyes-in-head during exploration producing misalignments of head and gaze. We have previously demonstrated in macaques that after a head-eye gaze shift the eyes and head tend to be aligned at the final position[46]. However, we tested marmosets during several sessions in which they were seated on a primate chair, and we fixed the head while they explored a visual scene on a computer monitor. We measured eye position and computed the amplitude and peak velocity of eye-in-head saccades. Interestingly, we observed that saccades were in their majority shorter than 5 degrees (**Fig. 2c, Fig. S1 e,f**), which coincides with the lower limit of the head movement distribution. So, if we were to estimate the gaze position from the head direction in the marmoset, the error could be as large as 5 degrees. Since our goal was not to obtain an accurate estimate of gaze position but to compare marmosets and rats' visual exploration strategies, we conclude our measurements have sufficient resolution to justify our main conclusions.

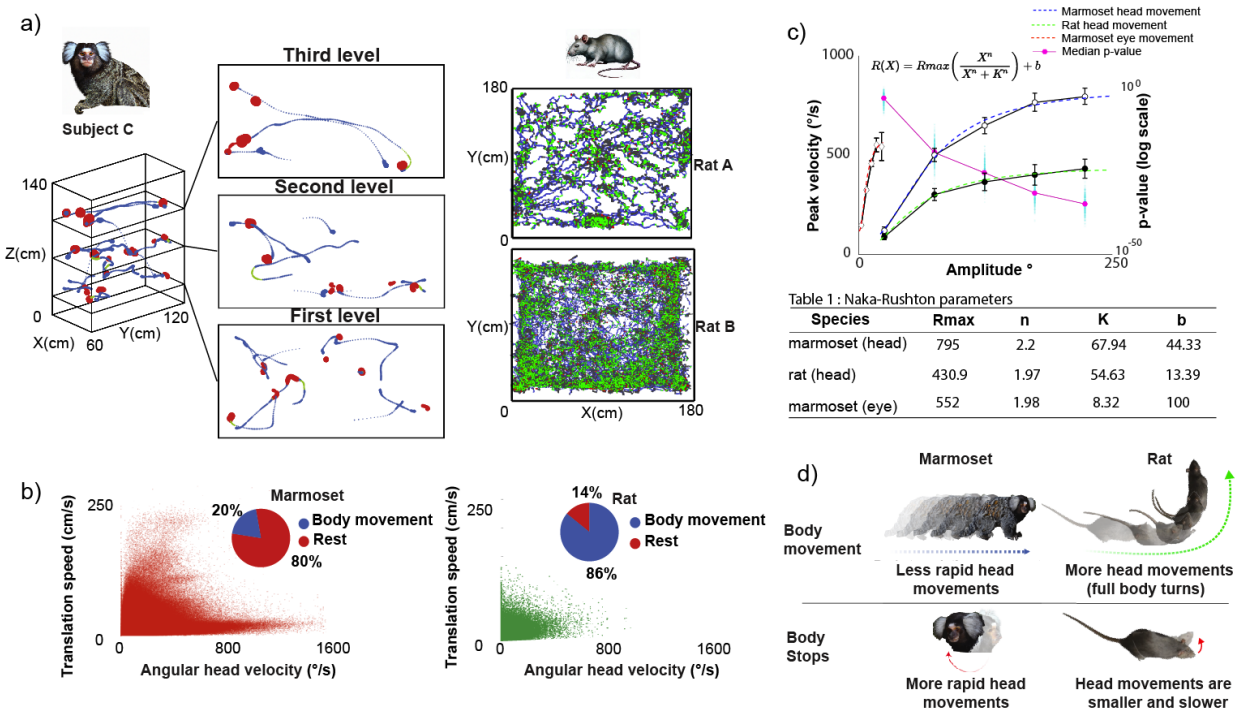

Figure 2 | Exploration strategies in marmosets and rats. (**a**) Selected trajectory examples of subject C (left) and 2 different rat subjects (right) during foraging (rat subject A on the top panel and rat subject B on the bottom panel). The size of the marker is proportional to the time spent at that location, Red = rapid head movement, Blue = body translation movement and Green = both head and body movement were present. (**b**) Distribution of AHV vs TS, pie chart displays the percentage of head movements that happen during body translation movement or rest (defined as no body movement present), for both marmoset (left) and rat (right). (**c**) Main sequence of head

movements for both marmoset (head and eye movements) and rat (head movements). A Naka-Rushton function was fit to the mean values (dashed line), Wilcoxon signed-rank test bootstrapped p-values (marmoset head movement data were re-sampled to match rat head movement counts, this process was repeated 500 times) are displayed on a log-scale (cyan dots) and median p-values are shown as pink line and dots. (**d**) Schematic of the two different exploration strategies observed in marmosets and rats during foraging.

Coding of space by single neurons in the freely moving marmoset hippocampus

We recorded the responses of single neurons and LFPs in the hippocampus of two common marmosets by implanting chronic microwire brush arrays (MBA, Microprobes for Life Science, Gaithersburg, MD) in the subfields CA3 (Subject P) and CA1 (Subject C). We verified the final position of the electrodes using 9.4T MRI and micro-CT imagining co-registration (**Fig. 3a**, **Fig. S2a**, and methods). Data acquisition was accomplished using wireless telemetry (CerePlex Exilis, Blackrock Microsystems, Salt Lake City, UT) while the marmosets foraged for rewards at reward ports of a 3D maze (**Fig. 3b** and methods). We defined view as the facing location of the marmoset at any given point in time (linear projection of the head direction onto the walls of the maze, see methods)[14]. We recorded a total of 331 neurons in both subjects (178 in subject C and 153 in subject P).

Excitatory pyramidal neurons are commonly regarded as the cells responsible for transmitting and processing spatial information in the hippocampus[1,50–52], while inhibitory interneurons have been associated with the encoding of non-spatial variables like speed[53], or with synchronizing activity in the hippocampal network[54]. To quantify spatial tuning to either place or view with conventional methods, we classified neurons based on their bursting properties and firing rate[55–59] into either putative interneurons or putative pyramidal cells (**Fig. 3c**), and we used exclusively putative pyramidal cells to assess variables related to spatial tuning. A total of 204 cells were classified as putative pyramidal and 127 were classified as putative interneurons.

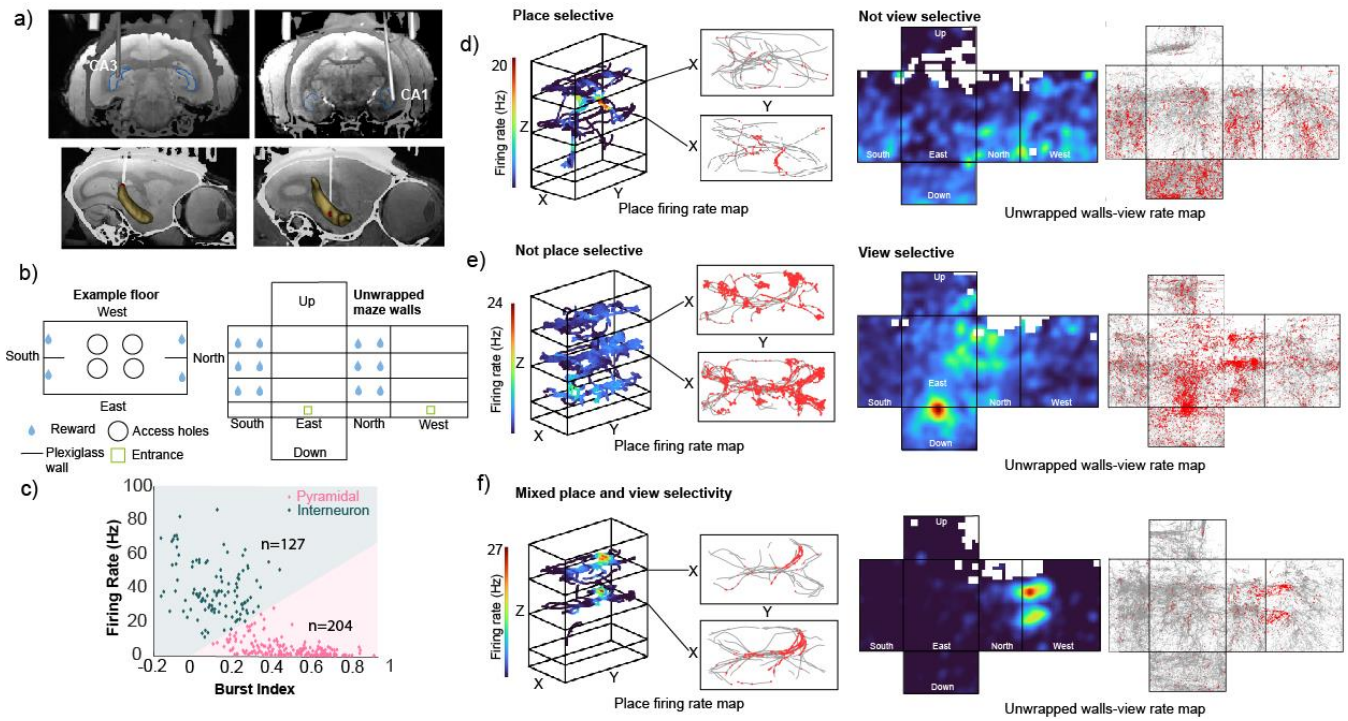

Figure 3 | Single neuron responses to view and place. (**a**) (top) MRI and CT imaging showing the final electrode location. (bottom) 3D reconstruction of the segmented hippocampus showing electrode location for Subject P (left) and Subject C (right). (**b**) Schematic representation of the 3D maze. (**c**) Electrophysiological parameters used to classify cells into putative pyramidal cells (n=204) or putative interneurons (n=127), the cluster boundaries are calculated using the k-means algorithm. (**d**) Single-cell example of a place cell. Firing rate maps for both place (left panels) and view (right panels). The color indicates the firing rate. (**e**) Single-cell example of a view cell (similar panel configuration as in d). (**f**) Single-cell example of a mixed place and view cell (similar panel configuration as in **d**).

Some putative pyramidal cells showed selectivity for the subject's position in the maze while they were poorly selective for view (example in **Fig. 3d**). Other cells show view selectivity but poor place selectivity (example in **Fig. 3e**). Other cells show a mix of view and place selectivity (example in **Fig. 3f**). For the analyses of spatial selectivity, we calculated the spatial information content (SIC)[60–62] of putative pyramidal cells. The SIC quantifies the amount of information (bits) each neuronal spike transmits about the location of the subject. SIC was computed for each putative pyramidal neuron, and a SIC shuffled control was computed by circularly shifting spike times by a random duration a total of 5000 times. Neurons with SIC that exceeded the 95th percentile of the null distribution were classified as selective. Overall, neurons had higher SIC for view than for place (**Fig 4b**, two-sided Wilcoxon signed-rank test, $p=1.4 \times 10^{-55}$, $Z=15.7$). Using this metric, we found that 66 (32%) of cells were place selective and 159 (76%) were view selective. For subject C, out of all the sampled view bins, 76.4% (99% confidence interval [64.5%, 88.4%]) had at least one cell that exhibited selectivity for that bin. Similarly, for subject P 78.3% (99% confidence interval [68.6%, 88%%]) had at least one selective view field. In contrast, of all visited place bins,

in both subjects, 25% (Subject C 99% confidence interval [12.11%, 36.1%], Subject P 99% confidence interval [14.1%, 34.2%]) had at least one selective place field.

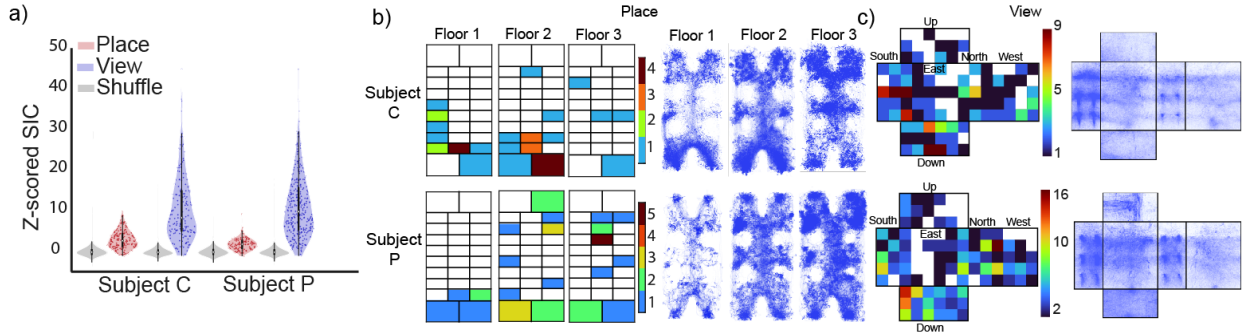

Figure 4 | SIC comparison between view and place and place/view field locations. (**a**) Violin distribution of Z-scored SIC for putative pyramidal cells, gray distribution is shuffled control. (**b**) (left) Place field location for all place cells and separated according to the three distinct floors of the 3D maze, color indicates the number of place fields at that location, white indicates bins without place fields. (right) Map of all spatial trajectories travelled across (n=26 and n=33 sessions) for subject C (top) and subject P (bottom), respectively. Color intensity reflects more time spent in that position. (**c**) View field locations for all view cells, color indicates the number of view fields at that location, white indicates bins without view fields. Right: map of all view-gaze positions (n=26 and n=33 sessions) for subject C (top) and subject P (bottom), respectively. Color intensity reflects higher counts.

Coding of speed by single neurons in the hippocampus of freely moving marmosets

Neurons in the rodent hippocampus show selectivity for the TS of the animal locomoting in a maze or running in a wheel[11,12,53,63–68]. However, little is known about the presence of speed cells in the hippocampus of non-human primates. A previous study[14] reported encoding of both TS and AHV in freely moving macaques, mainly in putative interneurons. We found no reports in the common marmoset.

For this analysis, we included both putative interneurons and pyramidal cells. We found single neurons that vary their response rate as a function of AHV (**Fig. 5a** left) and TS (**Fig. 5a** right). To quantify speed encoding we calculated the speed score as defined in[53,69] (Pearson correlation coefficient between the time series of firing rate and either AHV or TS). To select the neurons that were responsive to either AHV or TS, any given cell had to meet these two criteria: 1) as reported by a previous study[53], a speed score higher than 0.3, and 2) the cell's speed score had to be higher than the 95th percentile of speed scores in a shuffle null distribution (1000 permutations calculated by circularly shifting the vectorized spike raster relative to the equally sized speed vector) (**Fig. 5b, Fig. S2 e-h**). We found a total of 43 (33%) speed selective cells.

A significant amount of the speed cells encoded both, TS and AHV (**Fig. 5c**, 20 AHV cells, 3 TS cells, 20 mixed cells). Interestingly, neurons encoding AHV often show selectivity for only that variable, but most neurons encoding TS also showed selectivity for AHV (AHV cells 90% confidence interval [34%,59%]; TS 90% confidence interval [1%,13%]). As a control we investigated whether speed cells were predominantly putative interneurons (**Fig. 5 d, e**, **Fig. S2 i,**j,

proportion of speed cells that were putative pyramidal cells 90% confidence interval [3%,18%]; proportion of speed cells that were putative interneurons 90% confidence interval [82%, 97%]), furthermore, the median AHV and TS score for the population of putative interneurons was higher than in putative pyramidal cells (two-sided Wilcoxon signed-rank test, TS $p=3 \times 10^{-22}$, Z=9.7; AHV $p=1.3 \times 10^{-25}$, Z=10.5) corroborating that, as in the rat, speed tuned cells are mainly interneurons[53].

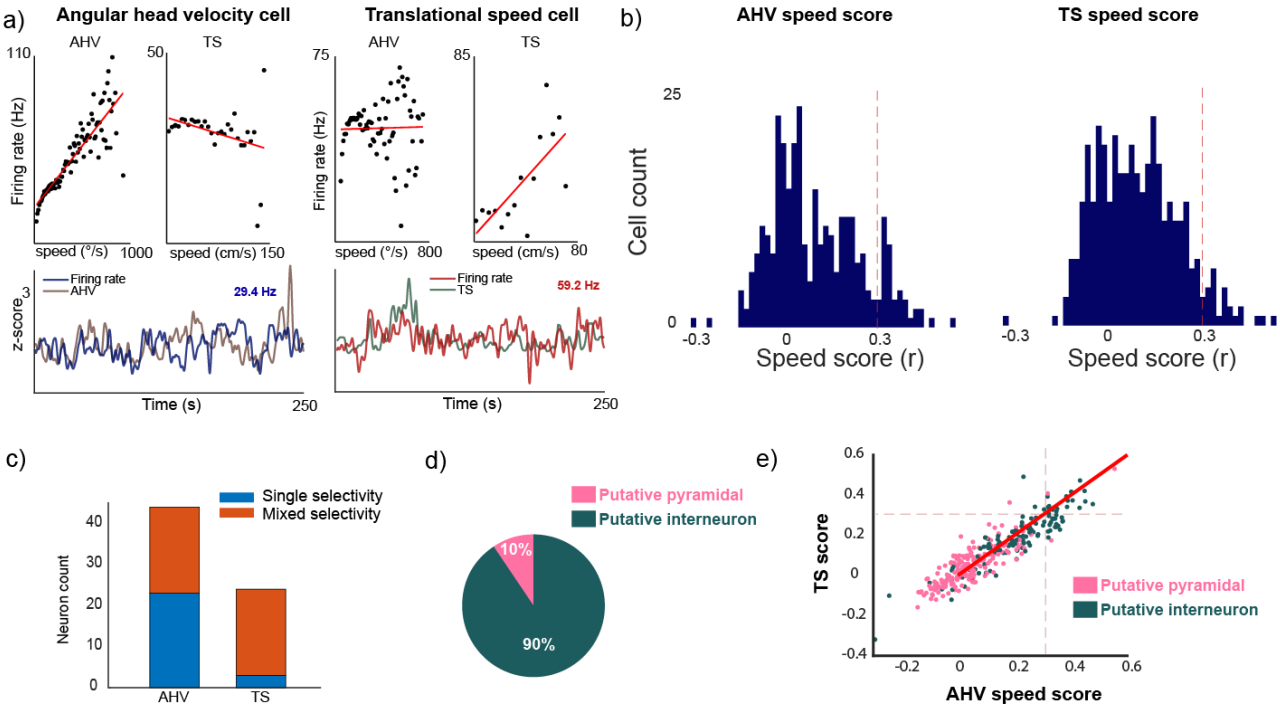

Figure 5 | Single neuron responses to TS and AHV. (a) Example cells. On the left for AHV, the cell increases the firing as a function of AHV but not TS. Right: TS cell firing increases as a function of TS but not AHV. **(b)** Distribution of speed score (Pearson correlation between time series of firing rate and speed) for both TS and AHV for all cells, the red dotted line at a 0.3-speed score, indicates the threshold to define significant encoding. **(c)** AHV and TS significant cells count distribution, orange color indicates cells that are both AHV and TS significant cells. **(d)** Distribution of speed cells according to putative cell type. **(e)** Speed score distribution for both AHV and TS labelled according to cell type, (green = putative interneuron, pink= putative pyramidal), the red dotted line indicates a speed score of 0.3.

Mixed selectivity in the marmoset hippocampus

To quantify mixed selectivity for the different variables (space, view, head direction and speed) in the recorded neurons we use a generalized additive model[70] (GAM) that fits the neuron's response to behavioral parameters described as the sum of fitted, cross-validated spline functions. We trained two different model types, one for putative pyramidal cells and the other for putative interneurons. The output model can have either none, one (first order model) or multiple variables (i.e. second or third order models) as significant predictors of the firing rate of single neurons, we can then classify cells that encode multiple variables as cells with mixed selectivity. For putative

pyramidal cells, the model included place, view, and head direction as predictors (**Fig. 6a**). The putative interneuron model included AHV and TS as predictors (**Fig. 6c**). Across all cell types, 160/331, 48.3% significantly encoded at least one variable (Putative pyramidal cells 56/204, 27.5%; Putative interneurons 104/127, 81.9%); amongst all encoding cells, mixed selectivity was predominant over single selectivity (140/160, 87.5% mixed selective; Putative pyramidal cells: 48/56, 85.7% mixed selective; Putative interneurons: 92/104, 88.5% mixed selective).

In the putative pyramidal model (**Fig. 6b**), place was exclusively encoded in combination with either view or head direction, there were no cells whose firing rate encoded only place, with the large majority of cells significantly encoding the three variables (view: 3/204, head direction: 5/204, view + head direction: 3/204, view + place: 3/204, place + head direction: 4/204, view + place + head direction: 38/204, **Fig. S4** for rate map examples, **Fig. S5 a,b** for individual marmoset results). For the putative interneuron model (**Fig. 6d, Fig. S5 c,d**), we found 6/127 (5%) AHV cells, 6/127(5%) TS speed cells and 92/127 (73%) mixed selective cells (AHV + TS). In summary, for the putative pyramidal model, single behavior selectivity is dominated by visuospatial variables (view + head direction) rather than place alone. For the putative interneuron model, selectivity was similar for TS and AHV. Finally, for both putative pyramidal and interneuron cells, mixed selectivity for combinations of different variables was predominant.

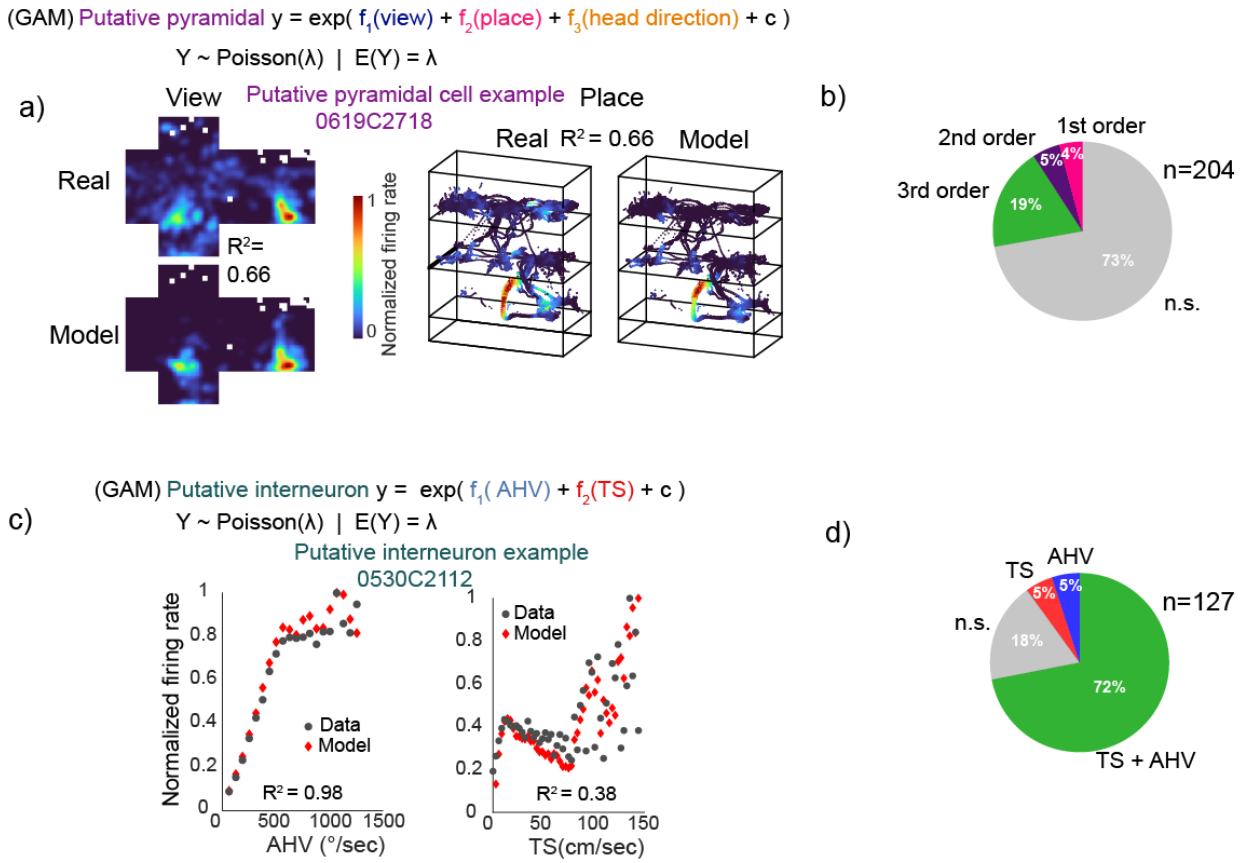

Figure 6 | Mixed selectivity GAM encoding model. A cross-validated GAM model was fitted to **(a)** putative pyramidal cells (view + place + head direction (h.d.)), single cell model fit example for view (left) and place (right), rate maps correlation shown as R^2. **(b)** Proportion of encoding putative pyramidal cells (pie chart). **(c)** GAM fitted to putative interneurons (AHV + TS), single cell model fit example for AHV (left) and TS (right), the goodness of fit is shown as R^2. **(d)** Proportion of putative interneuron encoding cells (pie chart).

Ensembles of mixed selective neurons encode place

Our previous results demonstrate that individual cells within the marmoset hippocampus are weakly selective for place, and rather encode a combination of variables, with a higher proportion of cells encoding view or head direction relative to place. This observation may suggest that the amount of place-related information in the marmoset hippocampus is relatively limited. However, previous research has demonstrated that populations of neurons, referred to as ensembles, can still contain substantial amounts of information about task-related variables, even if individual cells are poorly tuned [27,71,72]. Furthermore, numerous studies, conducted primarily in rodents have amassed a wealth of evidence demonstrating that the subject's position can be decoded from the firing rate of hippocampal cell ensembles[64,73,74] achieving accuracies of approximately 10cm (approximately equivalent to the subjects' body size)[75]. To further explore this issue, we used firing rates of a pseudo-population of mixed selective putative pyramidal cells in areas CA3 and CA1 to decode the animals' location in the maze.

We first divided the maze into two spatial regions (bins) per floor (**Fig. 7a**). From the 6 resultant bins, we identified the 4 bins that best optimized visitation frequency and neuron counts across all sessions for each subject, (**Fig. 7 a,d**; top). Using firing rates obtained during periods where the subject's head velocity was low (less than 200°/s, see methods), we decoded the subject's location employing a linear multiclass support vector machine (SVM) classifier. To identify the combination of neurons (ensemble) that provides the best decoding accuracy, we used an 'ensemble construction' method previously described[76,77]. We iteratively tested combinations of different neurons from a pool of a pseudo-population of putative pyramidal neurons. In the first iteration, we train one classifier per neuron, and the neuron exhibiting the highest decoding accuracy is then selected as the 'ensemble seed', for the second iteration, we train all the possible two-neuron combinations that include the previously selected units along with the remaining units in the pseudo-population; then the best two-neuron ensemble is selected. This process continued with each subsequent iteration, involving the training of an n+1 ensemble and the selection of the 'best ensemble', until performance becomes asymptotic (e.g., at n=20 cells). We constructed two different ensembles using this method, one where the pool of neurons included all recorded putative pyramidal cells, we called this the 'all units best ensemble' (pool size = subject C 75 cells, subject P 119 cells), and a second ensemble where the cells that significantly encoded at least one spatial variable, as per the previous GAM analysis, were excluded from the pool of neurons, we called this the 'no significant units best ensemble' (pool size = subject C 61 cells, subject P 78 cells). For both pools of neurons, we only included cells from sessions where subjects sampled each spatial bin at least 50 times. The latter was done to have sufficient data to train the classifiers. We fit a Naka-Rushton function to the decoder performance as a function of ensemble size and calculated statistics on the fit coefficients.

We decode place significantly above chance level (1/4, 0.25) ('all units best ensemble' decoding accuracy (**Fig. 7 a,d**; blue line, **Fig. 7 c,f**), subject C=0.45 (95% confidence interval [0.44 0.46]); subject P=0.49 (95% confidence interval [0.48 0.5]). The 'all units best ensemble' decoding accuracy was significantly higher than the 'no significant units best ensemble' decoding accuracy (**Fig. 7 a,d**; pink line), subject C=0.42 (95% confidence interval [0.41 0.43]); subject P=0.42 (95% confidence interval [0.41 0.43]). The latter indicates that neurons with significant fits for the GAM model contributed substantially to decoding accuracy. However, the fact that ensembles of neurons without significant fits also produce decoding accuracies higher than chance suggests that many of these neurons contain information about place. We further tested whether our ensemble construction method was effective in selecting combinations of the most informative neurons from the pseudo-population by training a decoder on 'random combination ensembles'. We randomly generated 100 different and unique combinations of 20 cells and decoded place from those ensembles (**Fig. 7 a,d**; cyan line). The 'random combination ensemble' decoding accuracy was significantly lower than the one of optimized ensembles, subject C = 0.35 (95% confidence interval [0.35 0.36]); subject P = 0.34 (95% confidence interval [0.34 0.35]).

Finally, we examined the encoding profiles of the neurons comprising the 'all units best ensemble'. Specifically, we focused on identifying the best-encoded spatial variable based on the GAM model. We found that the cells part of the ensemble encoded a mixture of view, head direction and place (**Fig. 7 b,e)**. Interestingly, despite place being the decoded variable, there is a predominance of view and head direction as the single cells' best-encoded variables in the 'optimized' ensembles. The latter demonstrates that spatial position could be decoded from our population of mixed selective neurons. Furthermore, it suggests that view and head direction can provide information about place and may explain the exploratory gaze behavior marmosets exhibit when stationary.

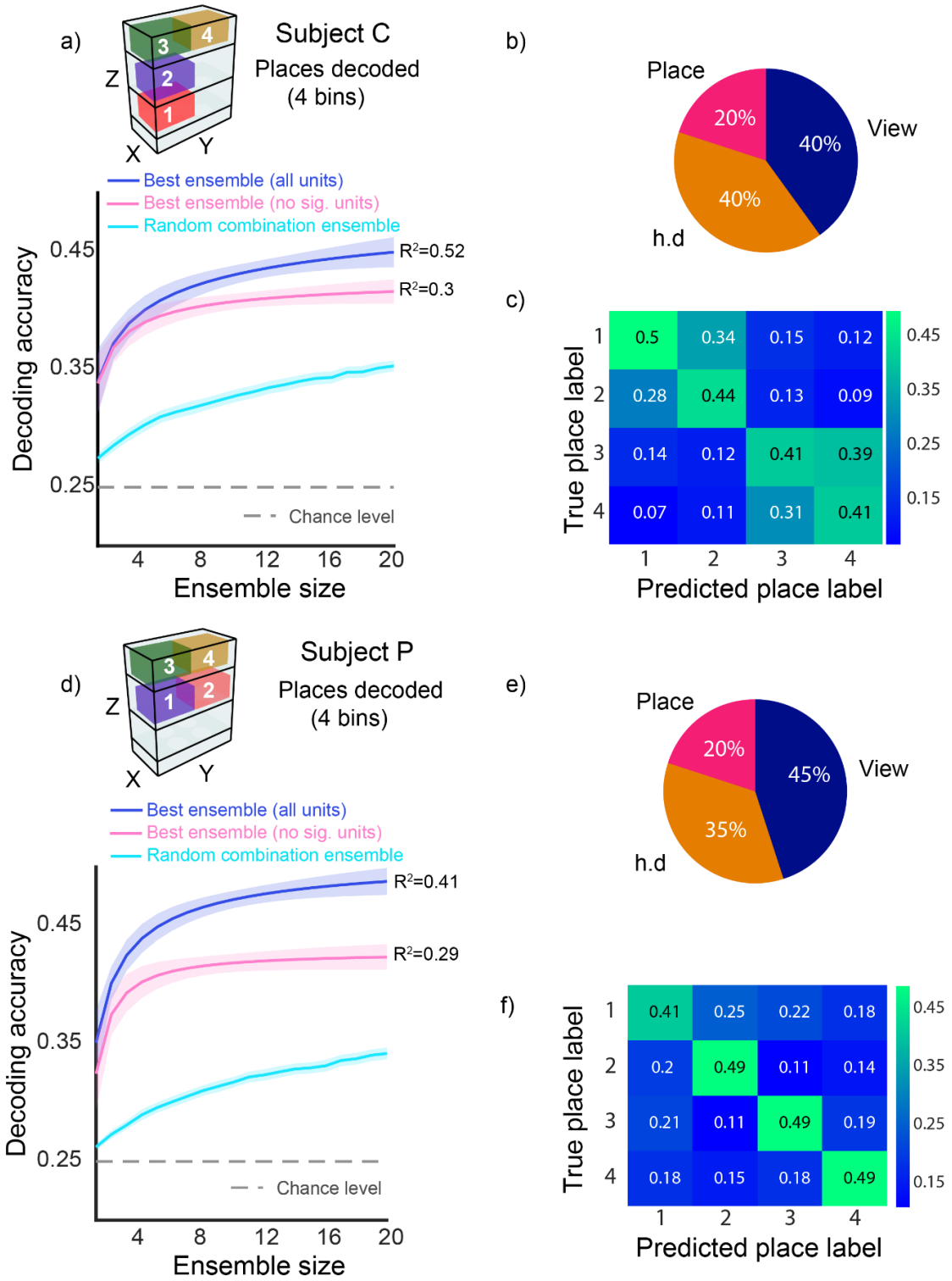
a)
Subject C
Places decoded
(4 bins)
Z
X
Y
1
2
3
4
Best ensemble (all units)
Best ensemble (no sig. units)
Random combination ensemble
Decoding accuracy
0.45
0.35
0.25
R²=0.52
R²=0.3
Chance level
4
8
12
16
20
Ensemble size
b)
Place
View
h.d
20%
40%
40%
c)
True place label
Predicted place label
1
2
3
4
0.5
0.34
0.15
0.12
0.28
0.44
0.13
0.09
0.14
0.12
0.41
0.39
0.07
0.11
0.31
0.41
0.45
0.35
0.25
0.15
d)
Subject P
Places decoded
(4 bins)
Z
X
Y
1
2
3
4
Best ensemble (all units)
Best ensemble (no sig. units)
Random combination ensemble
Decoding accuracy
0.45
0.35
0.25
R²=0.41
R²=0.29
Chance level
4
8
12
16
20
Ensemble size
e)
Place
View
h.d
20%
45%
35%
f)
True place label
Predicted place label
1
2
3
4
0.41
0.25
0.22
0.18
0.2
0.49
0.11
0.14
0.21
0.11
0.49
0.19
0.18
0.15
0.18
0.49
0.45
0.35
0.25
0.15

Figure 7 | Population decoding of place using a linear SVM classifier. (a,d) (top) 3D diagram of the binned place locations used to decode the subject's position, (bottom) blue and pink lines correspond to a Naka-Rushton function fit to the decoding accuracy (y-axis) as a function ensemble size (number of neurons, x-axis), shaded area corresponds to 95% confidence intervals. Blue solid lines correspond to the best ensemble constructed from a pool of all recorded putative pyramidal neurons. Pink solid lines correspond to the best ensemble constructed from a pool of non significantly selective cells (as per GAM encoding analysis). R^2 goodness of fit value is reported. The cyan lines correspond to the decoding accuracy of a randomized combination of neurons (100 iterations), shaded area corresponds to 95% confidence intervals. The gray dashed lines correspond to chance decoding accuracy (1/4, 0.25). **(b,e)** Best encoded variable proportion (as per GAM encoding analyses) for the combination of n=20 neurons part of the best ensemble pooled from all the single units (a,d; blue line). (**c,f**) Confusion matrix derived from the best ensemble classification accuracy (a,d; blue line).

Marmoset rapid head movements trigger LFP theta phase-resetting and modulation of single cell responses

Rhythmic, LFP theta oscillations in the hippocampus have been widely documented in rodents such as rats and mice[3,33]. Theta oscillations are thought to coordinate hippocampal cell assembles, and it has been proposed that they are involved in memory formation[78–80]. However, in some species like humans, macaques, marmosets, and bats, theta oscillations are not present as a rhythm during locomotion but appear in short bouts[14,15,81–83]. In humans and macaques, saccadic eye movements are thought to reset the phase of theta oscillations[35–37,84,85]. Here we hypothesize that head-gaze movements in the marmoset will induce theta phase resetting, which modulates neuronal activity during visual exploration (when the animals acquire information about the environment) aiding memory encoding.

We aligned the LFPs to the peak velocity of head movements (see methods) and computed average LFPs (**Fig. 8a**). We also aligned spectrograms corresponding to LFP traces and computed their averages. We found the strongest power in the 4-15Hz band with a peak at the theta frequencies (4-10Hz) around the onset of the head movement (**Fig. 8a**). To determine whether head-gaze theta phase-resetting was accompanied by a modulation of neuronal firing we obtained the average firing per single cell as a function of head movement events. We found that in both putative interneurons and pyramidal cells, spiking activity was modulated by the occurrence of a head movement (**Fig 7b, Fig. S6 d-f**). To quantify the precise nature of this modulation, we calculated a firing rate shuffled distribution through circular permutation of spike times, repeating the process 1000 times. Significance was evaluated using eight different bins, each spanning 50ms, within a 400ms window (total of eight bins). The center of the window was aligned with the peak velocity of each detected head movement event in the recording session, with a range of 200ms before and after the head movement peak velocity. Cells were classified as up-modulated if the real mean firing rate exceeded the 97.5^{th} percentile of the mean shuffle firing rate at that bin and across bins, down-modulated if the mean firing rate was lower than the 2.5^{th} percentile of the mean shuffle firing rate at any bin and across bins, and up/down modulated if their mean firing rate both exceeded and was lower than the 97.5^{th} and 2.5^{th} percentile of the shuffle respectively at different time bins.

We found that a lower percentage of putative pyramidal cells (72/204, 35.3%) were modulated (**Fig. 8c**) in comparison to putative interneurons (105/127, 82.7%). Furthermore, the average firing rate maxima of all modulated putative interneurons peaked at 31.2ms after the alignment 0 point (time from head movement velocity peak), whereas for all modulated putative pyramidal neurons it peaked at 81ms, a difference of 49.8ms. When accounting for the type of modulation (**Fig. 8d**), putative pyramidal cells seem more evenly split between down-modulation (14.7%) and up-modulation (19.6%), whereas, in modulated putative interneurons, up-modulation was most prevalent (66.9%), in comparison to down-modulation (6.3%). For both cell types, up/down-modulation was relatively rare at 1% in putative pyramidal and 9.5% in putative interneurons. The differences in activation latencies and the proportion of the different modulation types suggest that phase-resetting may be causally linked to interneuron activation that is followed by a range of modulation in pyramidal cells.

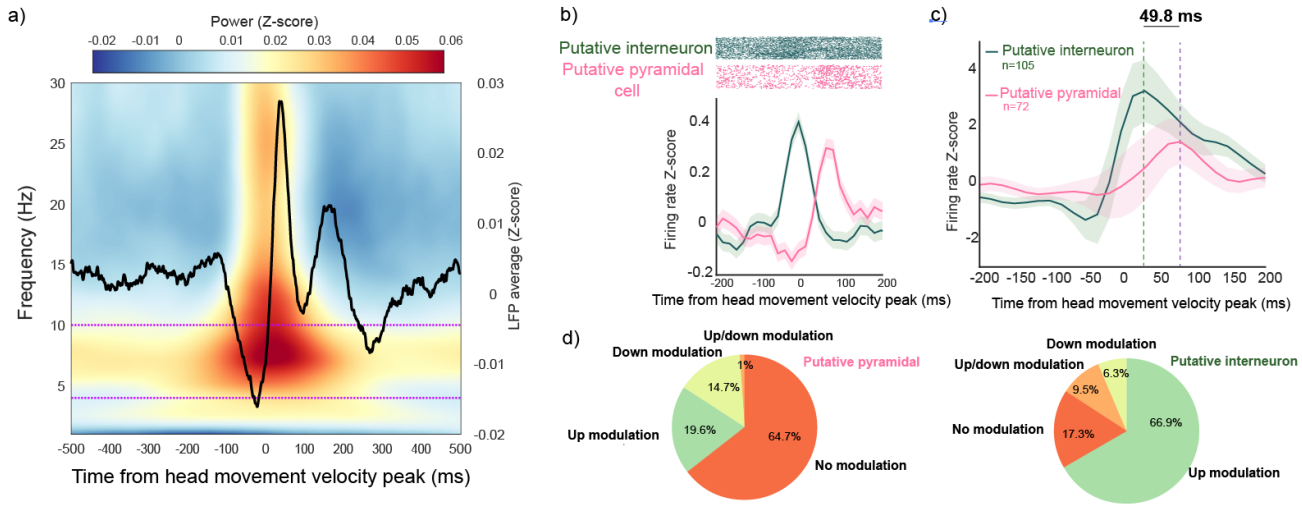

Figure 8 | Theta oscillations and single neuron phase-resetting to head movements. (a) Head-gaze phase-resetting of the average LFP aligned to head movement peak velocity (0 point). The color scale indicates average time-frequency representation (TFR) as Z-scored LFP power. Pink dotted lines indicate theta power band (4-10hz). **(b)** Single-cell phase-resetting example for a putative pyramidal (pink) and a putative interneuron (green) cell. **(c)** Average Z-scored firing rate phase-resetting for all head movement-modulated putative pyramidal (pink) and putative interneuron (green) cells; dotted line indicates the time of maximal activation. **(d)** Distribution of shuffle-controlled, head movement-modulated cells according to cell type (left, putative pyramidal; right, putative interneuron), cells can be up-modulated when the firing rate significantly increases, down-modulated when the firing rate significantly decreases, and up/down modulated when they show both significant increased and decreased phases (regardless of order).

Discussion

We used motion capture to track the behavior of freely moving marmosets foraging in a 3D maze and recorded the responses of neurons in the CA3 and CA1 regions of the hippocampus. We found that marmosets explore the environment using alternations of body translations and frequent stops. During translations head rotations are constrained. During stops, marmosets make frequent rapid

head-gaze shifts to explore the visual scene. This strategy differs from the one of rats, that frequently move their heads at low velocity 'scanning' the environment as they locomote. We found that putative pyramidal neurons in the CA3 and CA1 regions mainly encoded a mix of view, head direction, and place. Putative interneurons encoded a mix of AHV and TS. We demonstrated that the position of the animal in the maze (place) can be decoded from small ensembles of mixed selective cells, despite the predominance of encoding of view and head direction. Finally, we found that rapid head movements reset the phase of theta oscillations in the hippocampus. Theta phase-resetting is accompanied by the activation of interneurons followed by a variety of modulations in pyramidal cells.

Exploration strategies in marmosets and rats

Rats and mice have been the primary animal model used to study spatial navigation[86–89], with 1337 indexed publications in 2022 (Pubmed indexed search query: 'Rodentia' AND 'hippocampus/physiology'). Studies in non-human primates have been scarce (4 in 2022 in Pubmed indexed search, query: 'primates/physiology' OR 'Callithrix/physiology' OR 'Macaca mulatta' AND 'hippocampus/physiology'). There has been a tacit assumption that results from studies in nocturnal rodents such as mice and rats can be extrapolated to diurnal primates such as macaques and humans. However, there are differences between sensory systems and behaviours between nocturnal rodents and diurnal non-human primates that may be aligned with differences in how the hippocampus processes information during navigation. For example, rats and mice lack foveae, their eyes are displaced to the sides of the face, and they lack the wide range of color vision of diurnal primates like marmosets[26,90]. Rats can move their eyes independently, while marmosets cannot; marmosets make conjugate eye movements that preserve the alignment of the two eyes needed for stereovision[26,44]. Marmosets' high acuity color and stereovision allows far sensing during daylight to forage for fruit, trees, discriminate between conspecifics during mating or social interactions, or escape predators. These specializations make them distinct from nocturnal rodents such as rats.

Rapid head movements are key to marmosets' and other diurnal primates' efficient exploration of the environment via the far-sensing capabilities of their visual system[91]. They have previously been described in marmosets sitting in a primate chair[39]. In this study, we report the presence of these highly stereotypical movements in a marmoset navigating in 3D space. They followed the main sequence, much like it has been described for eye-head gaze shifts in macaques[46] and predominantly occur when the subjects are stationary, visually exploring the environment (visual navigation). We reasoned that because vision is 'far sensing' and the high-resolution fovea allows for the estimation of objects' features, animals do not need to actively visit locations to identify potential targets and landmarks for navigating. They can also identify depth stationary cues such as size differences, objects' occlusion cues, and dynamic cues using motion parallax that allow evaluating distances to target and path planning before translating in 3D space[92,93].

In contrast, mice and rats use a different strategy likely adapted to their nocturnal lifestyle. Their limited color vision, lack of a fovea and the absence of daylight may have evolved in the use of near-sensing capabilities to identify target objects during navigation and the lack of rapid head-gaze movements. Instead, they use slower head movements during navigation likely to position the whiskers or orient their olfactory apparatus toward possible targets or landmarks. In the

presence of poor illumination, rats would more frequently need to use path integration during self-motion for exploring the environment relative to marmosets.

The divergence between primates and rats may be traced to their ancestors. During early evolution, when mammals were predominantly nocturnal to escape predation by dinosaurs, most mammals regressed their visual capabilities, more suited for daylight, while expanding somatosensory, olfactory and hearing capabilities better suited for nocturnal activities[91]. However, primates may have escaped the pre-extinction nocturnal bottleneck by developing a sophisticated visual system, expanding the pathway from the retina to the thalamus and the visual cortex. This reliance on high-resolution stereo vision allowed foraging for insects and fruit in the distal branches of trees but may have produced a regression of their olfactory and somatosensory capabilities (e.g., whiskers). After the extinction of the dinosaurs, 66 million years ago, primates safely invaded the day-life niche further and disproportionally developed their already expanded visual system to incorporate color vision and extraordinary stereo and object recognition abilities[91]. This may have led primates, such as marmosets, to adopt more efficient navigation strategies relying on the far-sensing power of vision and consequently shaping neuronal selectivities in the hippocampus. In contrast, rats never escaped the nocturnal bottleneck and therefore, like their mammalian ancestor, preserved their near sensing capabilities such as whiskers, olfaction and audition to support navigation. Indeed, our data indicate that the common marmoset, a diurnal primate, uses different strategies to explore and navigate the environment compared to the rat, a nocturnal dweller. These differences may have impacted the physiological mechanisms of spatial navigation and specializations in the hippocampus of the two species.

Representation of space in the marmoset hippocampus

Previous studies in rats have shown that place cells form the basis for an internal representation of a spatial cognitive map[1,4]. The percentage of all hippocampal pyramidal cells that can be considered place cells ranges from 20-25%[4,94]. The identification of place cells in the rat hippocampus is astonishingly clear and replicable[1,4]. Studies in other species such as nocturnal bats have also reported place cells[82,95]. In primates, reports of place cells are scarce. Instead, studies using virtual reality in macaques have shown a representation of spatial locations that depend on objects-context[27] or landmarks[96]. A recent study in freely moving macaques[14] found that classic place cells are rare (7% of all cells). They reported that about 26% of all cells encoded place, but other variables such as facing location were better encoded. The only study in marmosets[15] showed that when subjects moved on a linear 'L-shaped' track, 14.1% of cells could be classified as place cells. Interestingly, they reported that 77.9% of these cells were directionally selective, which could be interpreted as encoding head direction or view, as in the macaque study[14].

Our study was conducted in freely moving marmosets in a 3D environment, where these small primates naturally forage. Although we found neurons that encoded view and place in the 3D maze, we show a predominance of variables related to the head direction and view. Place encoding occurred in 21.5% of all cells; however, we observed that place was exclusively encoded in conjunction with either view or head direction, and most frequently both. 'Bonafide' place cells as reported in rodents were not found.

Our results may be related to changes in the brain structure and function happening in diurnal primates such as the expansion of areas related to vision, and the emergence of a high-resolution fovea[91]. Diurnal primates have also evolved a sophisticated eye-head apparatus that allows coordinated gaze shifts to stabilize the fovea on objects of interest. Vision, as a far-sensing strategy has shaped diurnal primates' lifestyle and the physiology of the hippocampus. From an anatomical connectivity perspective, the primate hippocampus receives more visual information than that of the rat[97–101]; from a behavioral perspective, as shown in this study, there is a prevalence of navigation strategies that favor visual exploration behavior in primates. We argue that primate brains developed navigation and spatial memory systems adjusted to their diurnal lifestyles that heavily rely on visual cues and landmarks rather than on ma ps of space. One issue that remains unclear is whether the entire range of selectivities described as part of the navigational GPS in the entorhinal cortex of rodents (e.g., grid cells, border cells) is also present in primates. One study in macaques has described grid cell-like gaze selectivity in the entorhinal cortex when subjects inspected a visual scene[102]. This, however, is very different from grid cells that triangulate the animal's position in the environment.

Representation of speed in the marmoset hippocampus

While there is abundant evidence of speed-correlated activity in the hippocampus of rodents[11,12,53,63–68], there is limited evidence in primates. A study[14] reported significant encoding of both linear speed and angular velocity (TS and AHV in our study, respectively) in freely moving macaques, where most of these speed-encoding cells were putative interneurons. Similarly, a study found hippocampal cells in macaque monkeys, that responded to linear and rotation-assisted motion (monkey sitting in a remote-controlled robotic platform)[16]. Our study reports speed cells in the freely moving marmoset in a 3D environment. Moreover, we show that AHV was encoded to the same level as TS and that most cells had mixed selectivity for both variables. In agreement with rodent literature, the strongest speed-correlated signal was observed in putative interneurons[53].

One notable difference from findings made in rodents is the prevalence of AHV encoding in marmoset CA3/CA1 neurons. Encoding of AHV has been reported in rodent studies almost exclusively in either parahippocampal regions (MEC, parasubiculum, presubiculum)[103], retrosplenial cortex[104], or sub-cortical regions associated with vestibular information processing (lateral mammillary nuclei, thalamic nuclei and striatum)[7,8,105,106]. The encoding of AHV has been theorized that serves an essential role in the generation of grid cells[107,108] or the general processing of self-motion[69,109,110]. The function of head-speed cells in the marmoset is not clear but may be related to the signal that produces head-gaze theta phase-resetting.

Ensemble coding of space in the marmoset hippocampus

Our results demonstrate that space can be decoded from neuronal ensembles' firing activity in the hippocampus regions CA1/CA3 of marmosets (**Fig. 7**). Remarkably, the neurons that yield the highest decoding accuracy, are not highly selective to specific places. Instead, these neurons exhibit mixed selectivity for view, head direction and place (**Fig. 7 b,e**). Numerous prior work has explored how neuronal mixed selectivity supports efficient representation and processing of complex information in the brain [71,72,111]. Mixed selective neurons exhibit modest selectivity for

individual features, but increased selectivity for combinations of two or more features[111]. It has been theorized that neuronal ensembles face limitations to flexibly represent feature dimensions across different behavioral contexts when neuronal selectivity is highly specific[111]. This limitation becomes particularly prominent when considering that ensembles are constrained by a finite number of neurons. To overcome these limitations, neuronal networks may leverage between specificity and flexibility of neuronal selectivity[72]. This approach is especially advantageous when high-dimensional representations are required. Coding of space can be regarded as highly dimensional when encompassing a multitude of sensory inputs[61,112,113]. We propose that the presence of highly mixed information in the marmoset hippocampal neuronal ensembles supports reliable representations of space.

One contrasting difference between the neuronal responses observed in this study (and the NHP hippocampus in general), and the ones commonly observed in nocturnal rodents, is the predominance of variables directly related to gaze such as view and head direction[14,16,18,30]. Marmosets high-resolution foveal vision might allow anchoring of place representations and future paths for navigation to visual/scene cues, such as landmarks identity, depth, egocentric/allocentric location, and the spatial relationships between them extracted from visual exploration via gaze shifts[19]. In contrast, 'near' sensory cues like olfaction and whisking are readily available to nocturnal rodents such as rats. With heads positioned much lower above the ground relative to marmosets and a nocturnal lifestyle prioritizing places with poor illumination, rats may be 'less' visually-driven. However, recent work has demonstrated diverse selectivity in the hippocampus of rats; implementation of multivariate encoding analyses and novel experimental paradigms in previous studies provide evidence that place cells in the hippocampus of rats also encode variables beyond place, like position, distance and direction of motion of a bar of light under body fixed conditions[114], or be modulated by head direction and the presence of visual cues or olfactory cues[12,113,115,116]. Thus, mixed selectivity may be the norm in hippocampus neurons. However, mixed selectivity seems to be biased to overrepresent certain variables depending on the ecological niche of the species. For the case of marmosets, encoding of visual variables related to gaze orientation seems to be predominant in hippocampal neurons, at least in the daylight conditions in which diurnal primates usually forage.

Indeed, we found that place can be decoded from ensembles with a predominance of view and head direction mixed selective neurons. The information provided by these ensembles about landmarks in the environment (allocentric coding) and self-orientation relative to them (egocentric) can be sufficient to position oneself in space (origin of the place information) and aid goal-directed navigation[117] and the formation of spatial memories. It may also provide flexibility to adjust navigation strategies to the task demands (e.g., egocentric rather than allocentric representations[27]).

Head-gaze movement phase-resetting

It has been shown that memory encoding involves interactions between theta oscillations and incoming sensory signals into the hippocampus[118]. Indeed, responses of hippocampus neurons to sensory events are synchronized to a certain phase of theta oscillations[119,120]. It has been proposed that theta oscillations are like a metronome for coordinating sensory information transfer from cortical areas to the hippocampus[118]. This theory matches data from rodents; however, it has a

shortcoming when extrapolated to humans. In humans and non-human primates, hippocampus theta oscillations are not rhythmic but appear in short bouts[14,15,121,122]. Interestingly, some studies have reported that theta oscillations are locked to the execution of saccades[37], a phenomenon known as saccade phase-resetting[35].

Rapid head movements in species of primates are used to direct gaze toward spatial locations[24,46]. In marmosets head velocities reach values above that of eye velocities during saccades made with the head restrained (**Fig. 2c**). Here we report an LFP modulation described as head-gaze theta phase-resetting[22,37,84,123,124]. Moreover, a significant percentage of neurons' firing rate was modulated during and following head movement initiation. Notably, in putative interneurons the most common form of modulation was an increase in firing rate (up-modulation), but in putative pyramidal cells, it was evenly split between up and down modulation (**Fig. 8d**). The peak of the modulation effect was also found to be different across cell types, where putative interneuron modulation peaked before putative pyramidal cell (49.8 ms faster, **Fig. 8c**). Together, this suggests that the signal triggering head movements (e.g., a corollary discharge signal) initially activates interneurons that may reset background noise in pyramidal neurons that can be differentially activated by incoming sensory inputs.

We propose that head-gaze theta phase-resetting may act as a 'single pulse metronome' that synchronizes stochastic firing in neuronal ensembles before the eyes land on a target, allowing incoming sensory signals to be 'distinguished' from the background noise of the circuit. The activation of inhibitory interneurons may be causally linked to the process of resetting neuronal ensembles and decreasing noise, while the modulation in putative pyramidal neurons may be directly related to the arrival of sensory inputs to ensembles of pyramidal cells and encoding of sensory signals. This mechanism may be the driver of theta oscillations in diurnal mammals with foveal vision that explore the environment through voluntary gaze shifts. It has been further proposed that during a gaze shift a corollary discharge (CD) signal originating in the SC reaches the thalamus and then via the nucleus reuniens (NR) reaches the hippocampus[125,126]. However, a CD signal that reaches areas of the neocortex seems to do so via the medial dorsal thalamic nucleus[127] and plays roles such as inhibiting visual processing during saccades and remapping of receptive fields[127–130]. It is currently unclear how the CD signal in the hippocampus and neocortical areas are linked and how it relates to the head-gaze phase-resetting phenomenon reported here.

Conclusion

We provided evidence that freely moving marmosets use different exploration-navigation strategies compared to rats. These strategies have shaped physiological adaptations in the hippocampus. Cognitive maps of space in the marmoset and likely in other diurnal primates may be driven by mixed or conjunctive coding of gaze-related variables that enable encoding of visual features and object relationships used as landmarks for navigation. Head-gaze phase-resetting seems to play a role in synchronizing theta oscillations to increase the efficiency of information encoding in the marmoset hippocampus.

Data and code availability

The complete dataset and source code used in this study are available upon request to DBP or JCMT

Acknowledgements:

We thank registered veterinary technicians Kim Thomaes and Kristy Gibbs from Western University for technical assistance in surgeries and animal care; Kevin Barker from Neuronitek for design and manufacturing of implantable recording chambers and experimental set-up; Jonathan C. Lau from the Division of Neurosurgery, Western University for providing advice in neuro-navigation and targeting of deep brain structures; Stephen Frey from Rogue Research, Montreal, Canada for providing technical advice regarding microelectrode array implantation, neuro-navigation and manufacturing of custom microdrives; Megan Roussy from the Natural Sciences and Engineering Research Council of Canada (NSERC) for providing advice regarding spike sorting and data analysis; Gustavo Morrone Parfitt from Genentech, SF, CA, Borna Mahmoudian and Vaishnavi Sukumar for providing assistance during surgery and data collection; Joseph Umoh from Western University, for providing assistance with micro-CT imaging; Miranda Bellyou from Western University for providing assistance with 9.4 T MRI imaging. This work was supported by the Western University BrainsCAN award grant

Author contributions

DBP, JCMT, SC and CC designed and planned the study. DBP and JCMT planned and performed the surgeries. DBP collected, preprocessed and analyzed the data and created the figures for this manuscript. RAG developed code to quantify the SIC and provided expert knowledge guiding the data analysis and writing of this manuscript. BWC developed code to quantify and classify eye movements, quantify the burst index and provided expert knowledge to guide the data analysis and writing of this manuscript. LM provided expert knowledge to guide the analysis of time/frequency response in the LFP data. DBP and JCMT wrote and edited this manuscript.

Conflict of interest

The authors declare no conflict of interest.

Materials and Methods:

Ethics statement

The animal care and handling procedures, encompassing basic care, housing and husbandry, animal training, surgical procedures, and experiments (data collection), were granted approval by the University of Western Ontario Animal Care Committee. This approval guarantees adherence to federal (Canadian Council on Animal Care), provincial (Ontario Animals in Research Act), regulatory (e.g., CIHR/NSERC), and other national CALAM standards, ensuring the ethical use of animals. The animals' physical and psychological well-being was regularly assessed by researchers, registered veterinary technicians, and veterinarians.

Experimental setup and behavioral paradigm

Two adult (1 female, aged 5y and 1 male, aged 3y) marmosets were trained to forage for reward in a rectangular transparent maze with 3 different vertical levels (3D maze, **Fig. 1a**). For the majority of the recording sessions, the subjects were placed in the chamber alongside their cage partner with the purpose to alleviate stress. Reward locations were placed at 4 different positions in each level of the maze, two on one side and two on the opposite side (**Fig. 3b**). Each reward location consisted of a small panel containing an LED and a liquid reward delivery system controlled by a solenoid via the NIMH MonkeyLogic[131] software. The subject was cued by flashing the LED. When the subject approached the LED location and was closer than 15 cm to the reward delivery site a sound was played, and a reward was delivered. After that another, different LED was flashed, and the sequence of events was repeated. We also rewarded the subjects manually by waving a hand at the reward location and delivering a marshmallow when the subject approached. Recording sessions lasted for as long as the subject was willing to continue foraging (~40-60 minutes).

Motion capture 3D tracking

A total of 14, synchronized, cameras (Optitrack, Flex 13, Corvallis, OR), were placed around the 3D maze in a configuration that optimized coverage and minimized occlusion. Video frames were acquired at 60hz. The cameras emit 850nm infrared (IR) light and are fitted with a lens filter for IR light.

A recording chamber was placed on the skull of the subjects that allowed to house the electrodes and wireless recording headstage, a 3D printed cap covered the recording equipment and 6 spherical retro-reflective markers (4mm diameter, Facial Marker, Optitrack) were arranged in a unique geometric configuration (rigid body) and affixed on top of the cap.

Before every recording session, the setup was calibrated using a calibration wand (CWM-125, Optitrack). The wand consists of 3 markers of known dimensions and distance to each other that are used to compute a volumetric world coordinate system measured in metric units via triangulation algorithms. A calibration square (CS-100, Optitrack) was used to define the zero point (where the horizontal or X, depth or Y, and vertical or Z axes intercept) and the plane corresponding to the ground (plane parallel to the maze floors); the calibration square and subsequently the zero point was always placed at the lowest point of the south-west corner of the

maze. This calibration will be used by the tracking software (Motive, Optitrack) to compute the position and orientation of the cameras; the calibration step is essential to triangulate the 3D position (Xp, Yp and Zp, in metric units) of the markers from the individual camera's 2D images.

After the 3D position of the cluster of cap markers is estimated, the rigid body is tracked as a unique object at the pivot point (origin of the rotational axes roll, pitch and yaw), this point is manually placed at roughly the intersection between the vertical axis of the neck of the subject and the visual axis (eye level). The roll axis is manually aligned so that it is parallel to the estimated visual axis (red axis, **Fig. S1 a,b**), the pitch axis is manually aligned parallel to the maze floors (estimated using the ground plane, blue axis, **Fig. S1 a,b**) and the yaw axis is aligned parallel to the vertical plane (plane perpendicular to the ground plane, green axis, **Fig. S1 a,b**).

Implantation surgery and electrophysiological recordings

After co-registration of anatomical MRI (9.4T) and microCT (150um) scans[132–134] (3D Slicer software, slicer.org), we implanted a recording chamber 'cap' (**Fig. S1 i,h**) that allowed a 3D printed grid to be placed above the skull surface, each space in the grid could be used as a fiducial to calculate the trajectory necessary to reach the CA fields. We chronically implanted 32ch microwires 'brush' array electrodes in the hippocampus' CA1 (subject C) and CA3 (subject P) (Microprobes, Gaithersburg, USA). The final position of the electrodes was verified with post-surgical micro CT imaging and registration to the pre-surgical anatomical MRI (**Fig. 3a, Fig. S2a**). In subject P, we used a semi-chronic electrode implant that consisted of a small microdrive that allowed the electrode to be lowered after implantation (2 mm total range). We lowered the microdrive in increments of 70-150 um, until we reached the end of the working range and finally, took micro CT images to verify the final position of the electrode.

Neural activity was recorded using wireless telemetry (CerePlex Exilis, Cerebus Data Acquisition System, Blackrock Neurotech, Utah, USA) sampled at 30kHz.

Data Analyses

All analyses were performed using custom-built MATLAB scripts (Mathworks Inc**,** version 2021b) unless otherwise specified. A MATLAB wrapper was used to calculate the generalized additive models using PyGAM[70], a Python open-source resource.

Body translation speed

Translation speed or TS was defined as:

$$s = \frac{\sqrt{(\Delta x)^2 + (\Delta y)^2 + (\Delta z)^2}}{\Delta t}$$

Where s is the translation speed of the rigid body, x is the position in the horizontal axis, y is the position in the depth axis, z is the position in the vertical axis and t is time.

Angular head velocity

The rotation vectors (pitch, raw and roll) were exported from the motive software as rotation quaternions (q), defined as:

$$q = q_0 + iq_1 + jq_2 + kq_3$$

where q_0 , q_1 ,q_2 and q_3 are real numbers, and $\boldsymbol{i}$, $\boldsymbol{j}$ and $\boldsymbol{k}$ are imaginary unit vectors. Quaternions offer an advantage over traditional Euler's axis angles in that they are a more efficient way to compute rotations and are not susceptible to gimbal lock.

The AHV was defined as:

$$\omega = \frac{\Delta\theta}{\Delta t}$$

Where ω is the AHV, θ is the angular distance and t is time.

The angular distance θ between $\theta_{t2} - \theta_{t1}$ was computed using the MATLAB function *dist* (Robotics and autonomous systems toolbox).

Significant head and body movement classification

Significant head movements were defined as epochs where AHV was higher than 200°/s and the amplitude of the movement was higher than 10°. Movements with velocities higher than 2000°/s were deemed artifactual.

Significant body translations were defined as epochs where the TS was higher than 16 cm/s and the amplitude of the movement was at least 30cm. Movements with speeds higher than 300cm/s were deemed artifactual

Head Direction

We considered the distinction between head direction and view as illustrated by[135] (**Fig. S1h**)

The head direction is solved by the tracking software using a custom arrangement of markers that creates a rigid body with predefined XYZ axis angles. The axes are aligned to the subject's head anatomy and a pivot point is placed virtually in the neck, in a way that the horizontal head direction of the rigid body runs along the midline of the head and is parallel with the head direction and the vertical axis perpendicular to the maze floors.

The tracking software solves the head direction in terms of angular values of yaw (horizontal axis), pitch (vertical axis) and roll (lateral tilt axis) for the rigid body as a whole, in an allocentric reference frame.

The 2D head direction is estimated from the yaw angle values alone, and the 3D head direction is estimated from yaw, pitch and roll angles.

View as facing location

A ray is cast from the vector of 3D head direction and the intersection of this ray with the walls of the maze is defined as the facing location. Since the marmoset's oculomotor range is largely <10°, we interpret the facing location as view[26].

Signal pre-processing and spike sorting

Offline spike sorting was performed using Plexon (Offline Sorter, Plexon Inc., Texas, USA), a 4-pole, Butterworth, 250Hz high pass, a digital filter was applied to the raw 30kHz broadband signal, and a -4 sigma noise threshold was used to detect and align individual waveforms. Principal component analysis (PCA) was used to define the feature space and automatic (T-Distribution E-M) sorting was applied to isolate units. Manual inspection was then performed to classify units into noise units, multi-units or single-units (**Fig. S2 b,c,d**). Quality control measures were implemented after sorting the spike data. Single units that fired less than 100 spikes per session were invalidated. Additionally, to account for the use of microwire arrays where the final location of individual wires cannot be controlled, potential duplicate units were invalidated if the isolated units shared more than 50% of the spike times (estimated at 1ms temporal resolution). In cases where two or more units met this criterion, only the unit with the highest signal-to-noise ratio was included in the subsequent analyses.

Burst Index

Bursts can be described as a rapid sequence of action potentials followed by a period of relative quiescence[136,137], it has been estimated that 95% of pyramidal cells in the macaque monkey CA3 fire in bursts[138,139]. The burst index (BI) is a metric that has been proposed to describe the propensity of burstiness in the firing pattern of neurons, where higher BI values indicate a neuron's higher propensity to fire in bursts. As previously described[55,140] we calculated the BI by estimating both the inter-spike interval (ISI) histogram and the predicted ISI distribution, which is based on a Poisson distribution calculated from the mean firing rate of the whole recording session.

The predicted Poisson distribution of ISI was computed as follows:

$$f(t) = \lambda e^{-\lambda t}$$

Where λ= firing rate, and t= time bin. The probability was calculated for each 1ms time bin in the 2-40ms time range, a normalization procedure was implemented by summing all of the predictions in both the predicted and real ISIs.

The burst index was computed as the following:

$$burst\ index = \frac{\sum ISIs\ measured\ - \sum ISIs\ predicted}{\sum ISIs\ measured\ + \sum ISIs\ predicted}$$

Where the sum of ISIs was performed between the values from 2 and 20ms. The burst index is ultimately defined as the division between the subtraction of the measured ISI sum and the ISI predicted, and the sum of both these sums. In the end, the index is bound between -1 and 1.

Classification of putative interneuron and pyramidal cells

Macaque monkey hippocampal neurons have been putatively classified as interneuron/pyramidal cells based on firing rate alone[56,58], where interneuron cells are typically of the fast-spiking type (average firing rates above 10Hz). To increase the robustness of classification in our analysis and avoid potential species-specific biases that firing rate thresholding classification could introduce (since it has only been used in macaque monkeys), we implemented an unsupervised classification algorithm (k-means, MATLAB function *kmeans*) using burst index and average firing rate as features. We refrained from using other classical methods of classification like spike waveform width, since it has been shown that short-duration waveforms from neurons recorded from the hippocampus can represent axonal activity, and are not necessarily inhibitory interneurons in nature[57].

Spatial information content

Occupancy and firing rate maps were estimated based on a spatial bin division shown in **Fig.4 b,c**, (place bins n=84, view fields n=106) per recording session. Bins that weren't sampled more than 3 independent times, or less than 200ms were discarded. Spatial Information Content (SIC)[61,62] was calculated independently for place and view for every individual cell. SIC was defined as:

$$I = \sum_{i}^{L} P_i \frac{\lambda_i}{\bar{\lambda}} \log_2 \frac{\lambda_i}{\bar{\lambda}}$$

Where the proportion of occupied time in each spatial bin is (P_i) and λ is the mean firing rate.

Significant cells were defined as SIC > 0.05 (corrected alpha value for the number of bins) of the null distribution (5000 circular shift permutations). In the same way, for significant cells, significant bins (place or view fields) were defined as SIC > 0.05 (corrected alpha value for the number of bins) of the null distribution for that bin.

Speed cell definition

A single cell was defined as a speed cell if it met two criteria:

1) Speed score higher than 0.3:

We used the same definition as[53,69], for the speed score, which is the Pearson's correlation coefficient between the time series of speed and the time series of firing rate.

After determining the instantaneous speed (sampled at 60hz), both the time series of speed (AHV and TS were computed independently) and firing rate were smoothed using a 1-D Gaussian with 50ms standard deviation. The correlation coefficient was defined as the following:

$$r = \frac{\sum(x_i - \bar{x})\,(y_i - \bar{y})}{\sqrt{\sum(x_i - \bar{x})^2 \sum(y_i - \bar{y})^2}}$$

and it was calculated using the MATLAB function corrcoef.

2) Shuffle control criteria

Using the same smoothed firing rate time series, a shuffle distribution of speed scores was computed after circularly shifting the time series 1000 times. This distribution served as the null distribution used to estimate the significance of the real speed score (real speed score higher than 95th percentile null distribution).

Since AHV and TS speed scores are estimated independently, cells can be classified as AHV cells, TS cells, or both.

Generalized Additive Model (pyGAM)

Generalized additive models (GAM) are a particularly useful tool to explore the relationship between neural activity and multiple behavioral variables. They are specifically advantageous when exploring complex and non-linear interactions between the covariates and the independent factor[141]. Here we describe the implementation used in every neuron reported in the paper, we used this model to classify single cells according to their encoding profiles; where a cell could significantly encode none, one or a combination of behaviours (predictors).

The general form of GAMs is described by:

$$F(x) = y = exp(\beta_0 + f_1(x_1) + f_2(x_2) + \ldots + f_r(x_r))$$

In our implementation y is a single neuron's firing rate, β_0 is the intercept (constant), $[X_1, X_2, \ldots X_r]$ are the predictor variables (space, view, head direction and speed).

This GAM implementation has three components: distribution, link function ($F(x) = g(\mu|X)$) and a functional form (f_r). We calculated all our models using a log link function, Poisson distribution and a functional form function of penalized B splines[142]. The models are cross-validated during training to avoid overfitting, and the goodness of fit estimates are averaged across k-folds.

As reported in the results section, spatially selective cells are mainly putative pyramidal cells and speed-encoding cells are mainly putative interneurons, so in order to optimize computing times, we designed two separate models, one for putative pyramidal neurons (including space, view and head direction) and the other for putative interneurons (AHV and TS).

We utilized a nested, stepwise, forward search model selection approach to determine the optimal number of predictors per cell (**Fig. S3a**). The methodology involved a gradual construction of the model by iteratively incorporating predictor variables based on their individual contributions to the overall goodness of fit. Initially, all available one-variable models (first-order models) were fitted, and a surrogate null distribution of first-order models was computed. This null distribution was obtained by randomly circularly shifting the vectorized firing rate a total of 50 times. To establish statistical significance, we compared the actual explained deviance (ED) with the 95th percentile of the null distribution (Bonferroni corrected). If the real ED exceeded this threshold, the model was considered statistically significant.

The ED of the real model was then normalized by subtracting the mean shuffle ED from the real ED, allowing us to select the first-order model with the highest ED when multiple first-order models crossed the significance threshold. The variable in the best model was retained as a predictor for the subsequent iteration of model selection (n+1 order model). In each iteration, one

of the remaining variables was added at a time until all combinations of that order were evaluated. Similar to the first-order models, statistical significance was assessed by comparing it against a null shuffle distribution. For models with more than one variable, the time series of the single predictor under consideration was circularly shuffled, while the firing rate and already selected predictors remained unaltered. The training process concluded when the incremental improvement in model fit by adding more variables became statistically negligible. At this point, the final combination of variables was selected as the best model for a specific neuron.

The performance of the winning model is evaluated by generating a spike raster prediction using the best final nested GAM model (**Fig. S3 b,c**). These predictions are then compared to the actual neuron's rasters using cross-validation with 5 folds. Since each recording session (40-60 minutes long) is divided into 5 equally-timed folds, each predicted raster is a continuous time series approximately 8-12 minutes long. To assess the similarity between the predictions and the real rasters, the Pearson correlation coefficient is calculated between the predicted and real raster data. Additionally, the coefficient of determination (R^2) is obtained for each fold, and the final R^2 is computed by averaging across all folds(**Fig. S5 a,c**).

To determine the statistical significance of the model's predictive power, an F-test is performed on the calculated R^2 values, using an α-value of 0.05. This test allows us to ascertain if the model's performance is significantly better than what would be expected by chance. Cells whose winner model's performance is statistically significant are considered to encode the variables used as predictors in that model.

Place decoding analyses

We used a linear multi-class support vector machine (SVM) classifier (*fitecoc,* MATLAB function), composed of ‘n’ number of classes of binary learners in a one-versus-one design. The performance accuracy of each model was evaluated using 5-fold cross-validation and trained 10 times using distinct subsamples of all available trials. The subsampling procedure ensured the proper balance of classes with varying trial numbers. The model’s features were derived from firing rates of a pseudo-population of neurons, obtained from periods where the AHV was lower than 200°/s, akin to head ‘fixations’, which in marmosets can be considered analogous to eye fixations. The firing rates were integrated over 200ms centred around those low AHV periods; each interval was treated as a trial. We included neurons in the pseudo-population if they had samples from a spatial bin (see below) at least 50 times (trials) per recording session.

To decode place from this pseudo-population, we partitioned the maze into 2 spatial bins per floor, resulting in a total of 6 spatial bins. We identified the 4 spatial bins (the model’s classes) with the highest visitation frequency and number of neurons that could be incorporated into the pseudo-population (**Fig. 7 a,d)**.

We used a previously described ensemble construction procedure[76,77], this procedure iteratively finds the combination of neurons that provides the best decoding performance from a pool of pseudo-population of neurons (**Fig. S5e**). First, we train all the single-neuron models and identify the model with the highest decoding accuracy. We use this neuron as the ‘seed’, and we fit all possible combinations of n+1 ensembles including the seed and the remaining neurons in the pool. We then select the sub-ensemble with the highest decoding accuracy and continue fitting n+1

models with the remaining units. We repeat this procedure until the performance of the model becomes asymptotic and does not significantly improve by adding more units; this final ensemble was referred to as the 'all units best ensemble'. To evaluate the contribution of the neurons that significantly encode spatial variables, as per the GAM analysis, we repeated the previous ensemble construction procedure while excluding those neurons from the pool. We referred to this ensemble as the 'no significant units best ensemble'. Finally, we fit a Naka-Rushton function to both ensembles' performance, to calculate statistics on the fit coefficients and to aid with visualization. Raw ensemble performances can be found in the supplementary information (**Fig. S6 a,b**)

To validate the efficacy of the ensemble construction procedure in identifying the 'optimal' combination of neurons that maximized the classifier's performance, we fit a 'random combination ensemble', where we randomly generated 100 different combinations of neurons from the pseudo-population pool. Subsequently, we iteratively trained the model using n+1 neurons from the randomly generated combination.

Signal pre-processing for local field potentials

Using the FieldTrip toolbox[143] a 4-pole, Butterworth, 250Hz high pass digital filter was applied to the raw 30kHz broadband signal. The data was then down-sampled to 1kHz. To eliminate low-frequency noise a 1Hz high pass filter was applied and a high-frequency artifact rejection algorithm was employed where the data was band-pass filtered between 100-250Hz (9-order Butterworth filter and boxcar of 0.2) and the Hilbert envelope of the signal was calculated and subsequently Z-scored. The artifact threshold was defined at 4 Z-score and a window including 100 ms before and after threshold crossing was rejected.

Time-frequency representation

To calculate the oscillatory power of the LFP and its time-frequency representation, we used Morlet wavelets, implemented with the FieldTrip toolbox. The wavelets consisted of 7 oscillations, with center frequencies ranging from 1 to 30Hz (in even steps of 1Hz), and a 25ms smoothing time window. Baseline normalization was implemented to account for 1/f activity using the decibel conversion method, described as follows:

$$\mathrm{dB} = 10\log_{10}\left(\frac{signal}{baseline}\right)$$

Where the baseline was estimated as the fractal component from the power spectrum calculated using the Fitting Oscillations and One-Over-F (FOOOF) algorithm[144] (FieldTrip implementation).

Neuronal modulation to head movements

Our classification of modulated units builds upon the framework presented in the work of a previous study[126]. However, our approach differs in that we introduce an additional category of modulation, namely units that are both up and down-modulated.

Spike timestamps for a given single neuron are exported from the Plexon software as binary spike trains with a 1ms time resolution. We extracted spike train epochs (a window of 400ms) centered on the peak velocity of head movements and divided that window into 8 equally timed bins (50ms each). We calculated average spike rates across all head movements for each bin. Next, we

generated a shuffled distribution of firing rates by circularly permutating spike times, repeating this process 1000 times. Cells were classified as up-modulated if the real average firing rate exceeded the 97.5th percentile of the shuffle average firing rate at any bin and across bins (shuffle distribution of maximum firing rates across the entire 400ms window). Cells were classified as down-modulated if the real average firing rate was lower than the 2.5th percentile of the shuffle at any bin and across bins (shuffle distribution of minimum firing rates across the entire 400ms window). Cells were classified as up/down modulated if their real average firing rate both exceeded the 97.5th percentile and was lower than the 2.5th percentile of the shuffle at different time bins.

References:

1. O'Keefe, J. & Dostrovsky, J. The hippocampus as a spatial map. Preliminary evidence from unit activity in the freely-moving rat. *Brain Res.* **34**, 171–175 (1971).
2. Morris, R. G. M., Garrud, P., Rawlins, J. N. P. & O'Keefe, J. Place navigation impaired in rats with hippocampal lesions. *Nature* **297**, 681–683 (1982).
3. Buzsáki, G. & Moser, E. I. Memory, navigation and theta rhythm in the hippocampal-entorhinal system. *Nat. Neurosci.* **16**, 130–138 (2013).
4. O'Keefe, J. & Nadel, L. *The Hippocampus as a Cognitive Map*. *Oxford University Press: Oxford, UK. (1978)* (Oxford University Press, 1978).
5. Taube, J. S., Muller, R. U. & Ranck, J. B. Head-direction cells recorded from the postsubiculum in freely moving rats. I. Description and quantitative analysis. *J. Neurosci. Off. J. Soc. Neurosci.* **10**, 420–435 (1990).
6. Taube, J. S., Muller, R. U. & Ranck, J. B. Head-direction cells recorded from the postsubiculum in freely moving rats. II. Effects of environmental manipulations. *J. Neurosci. Off. J. Soc. Neurosci.* **10**, 436–447 (1990).
7. Taube, J. S. Head direction cells recorded in the anterior thalamic nuclei of freely moving rats. *J. Neurosci. Off. J. Soc. Neurosci.* **15**, 70–86 (1995).
8. Stackman, R. W. & Taube, J. S. Firing properties of head direction cells in the rat anterior thalamic nucleus: dependence on vestibular input. *J. Neurosci. Off. J. Soc. Neurosci.* **17**, 4349–4358 (1997).
9. Hafting, T., Fyhn, M., Molden, S., Moser, M.-B. & Moser, E. I. Microstructure of a spatial map in the entorhinal cortex. *Nature* **436**, 801–806 (2005).

10. Moser, E. I., Kropff, E. & Moser, M.-B. Place cells, grid cells, and the brain's spatial representation system. *Annu. Rev. Neurosci.* **31**, 69–89 (2008).

11. McNaughton, B. L., Barnes, C. A. & O'Keefe, J. The contributions of position, direction, and velocity to single unit activity in the hippocampus of freely-moving rats. *Exp. Brain Res.* **52**, 41–49 (1983).

12. Wiener, S. I., Paul, C. A. & Eichenbaum, H. Spatial and behavioral correlates of hippocampal neuronal activity. *J. Neurosci. Off. J. Soc. Neurosci.* **9**, 2737–2763 (1989).

13. Sargolini, F. *et al.* Conjunctive Representation of Position, Direction, and Velocity in Entorhinal Cortex. *Science* **312**, 758–762 (2006).

14. Mao, D. *et al.* Spatial modulation of hippocampal activity in freely moving macaques. *Neuron* **109**, 3521-3534.e6 (2021).

15. Courellis, H. S. *et al.* Spatial encoding in primate hippocampus during free navigation. *PLOS Biol.* **17**, e3000546 (2019).

16. Rolls, E. T. & O'Mara, S. M. View-responsive neurons in the primate hippocampal complex. *Hippocampus* **5**, 409–424 (1995).

17. Rolls, E. T. Spatial view cells and the representation of place in the primate hippocampus. *Hippocampus* **9**, 467–480 (1999).

18. Corrigan, B. W. *et al.* View cells in the hippocampus and prefrontal cortex of macaques during virtual navigation. *Hippocampus* **33**, 573–585 (2023).

19. Wirth, S. A place with a view: A first-person perspective in the hippocampal memory space. *Hippocampus* **33**, 658–666 (2023).

20. Rolls, E. T. Hippocampal spatial view cells, place cells, and concept cells: View representations. *Hippocampus* **33**, 667–687 (2023).

21. Felleman, D. J. & Van Essen, D. C. Distributed hierarchical processing in the primate cerebral cortex. *Cereb. Cortex N. Y. N 1991* **1**, 1–47 (1991).

22. Meister, M. L. R. & Buffalo, E. A. Getting directions from the hippocampus: The neural connection between looking and memory. *Neurobiol. Learn. Mem.* **134 Pt A**, 135–144 (2016).

23. Rolls, E. T. & Wirth, S. Spatial representations in the primate hippocampus, and their functions in memory and navigation. *Prog. Neurobiol.* **171**, 90–113 (2018).

24. Klier, E. M., Wang, H. & Crawford, J. D. Neural mechanisms of three-dimensional eye and head movements. *Ann. N. Y. Acad. Sci.* **956**, 512–514 (2002).

25. Martinez-Trujillo, J. C., Medendorp, W. P., Wang, H. & Crawford, J. D. Frames of Reference for Eye-Head Gaze Commands in Primate Supplementary Eye Fields. *Neuron* **44**, 1057–1066 (2004).

26. Mitchell, J. F., Reynolds, J. H. & Miller, C. T. Active Vision in Marmosets: A Model System for Visual Neuroscience. *J. Neurosci.* **34**, 1183–1194 (2014).

27. Gulli, R. A. *et al.* Context-dependent representations of objects and space in the primate hippocampus during virtual navigation. *Nat. Neurosci.* **23**, 103–112 (2020).

28. Killian, N. J. & Buffalo, E. A. Grid cells map the visual world. *Nat. Neurosci.* **21**, 161–162 (2018).

29. Feigenbaum, J. D. & Rolls, E. T. Allocentric and egocentric spatial information processing in the hippocampal formation of the behaving primate. *Psychobiology* **19**, 21–40 (1991).

30. Rolls, E. T., Robertson, R. G. & Georges-François, P. Spatial View Cells in the Primate Hippocampus. *Eur. J. Neurosci.* **9**, 1789–1794 (1997).

31. Ludvig, N., Tang, H. M., Gohil, B. C. & Botero, J. M. Detecting location-specific neuronal firing rate increases in the hippocampus of freely-moving monkeys. *Brain Res.* **1014**, 97–109 (2004).

32. Hazama, Y. & Tamura, R. Effects of self-locomotion on the activity of place cells in the hippocampus of a freely behaving monkey. *Neurosci. Lett.* **701**, 32–37 (2019).

33. Vanderwolf, C. H. Hippocampal electrical activity and voluntary movement in the rat. *Electroencephalogr. Clin. Neurophysiol.* **26**, 407–418 (1969).

34. Eliav, T. *et al.* Nonoscillatory Phase Coding and Synchronization in the Bat Hippocampal Formation. *Cell* **175**, 1119-1130.e15 (2018).

35. Doucet, G., Gulli, R. A., Corrigan, B. W., Duong, L. R. & Martinez-Trujillo, J. C. Modulation of local field potentials and neuronal activity in primate hippocampus during saccades. *Hippocampus* **30**, 192–209 (2020).

36. Andrillon, T., Nir, Y., Cirelli, C., Tononi, G. & Fried, I. Single-neuron activity and eye movements during human REM sleep and awake vision. *Nat. Commun.* **6**, 7884 (2015).

37. Hoffman, K. *et al.* Saccades during visual exploration align hippocampal 3–8 Hz rhythms in human and non-human primates. *Front. Syst. Neurosci.* **7**, (2013).

38. Arkley, K., Grant, R. A., Mitchinson, B. & Prescott, T. J. Strategy change in vibrissal active sensing during rat locomotion. *Curr. Biol. CB* **24**, 1507–1512 (2014).

39. Pandey, S., Simhadri, S. & Zhou, Y. Rapid Head Movements in Common Marmoset Monkeys. *iScience* **23**, 100837 (2020).

40. Mizuseki, K., Sirota, A., Pastalkova, E. & Buzsáki, G. Theta oscillations provide temporal windows for local circuit computation in the entorhinal-hippocampal loop. *Neuron* **64**, 267–280 (2009).

41. Leinonen, H. & Tanila, H. Vision in laboratory rodents-Tools to measure it and implications for behavioral research. *Behav. Brain Res.* **352**, 172–182 (2018).

42. Reinagel, P. Using rats for vision research. *Neuroscience* **296**, 75–79 (2015).

43. Samonds, J. M., Choi, V. & Priebe, N. J. Mice Discriminate Stereoscopic Surfaces Without Fixating in Depth. *J. Neurosci.* **39**, 8024–8037 (2019).

44. Wallace, D. J. *et al.* Rats maintain an overhead binocular field at the expense of constant fusion. *Nature* **498**, 65–69 (2013).

45. Bahill, A. T., Clark, M. R. & Stark, L. The main sequence, a tool for studying human eye movements. *Math. Biosci.* **24**, 191–204 (1975).

46. Martinez-Trujillo, J. C., Wang, H. & Crawford, J. D. Electrical Stimulation of the Supplementary Eye Fields in the Head-Free Macaque Evokes Kinematically Normal Gaze Shifts. *J. Neurophysiol.* **89**, 2961–2974 (2003).

47. Knutsen, P. M., Pietr, M. & Ahissar, E. Haptic Object Localization in the Vibrissal System: Behavior and Performance. *J. Neurosci.* **26**, 8451–8464 (2006).

48. Towal, R. B. & Hartmann, M. J. Right–Left Asymmetries in the Whisking Behavior of Rats Anticipate Head Movements. *J. Neurosci.* **26**, 8838–8846 (2006).

49. Meier, R. K. & Dieringer, N. The role of compensatory eye and head movements in the rat for image stabilization and gaze orientation. *Exp. Brain Res.* **96**, 54–64 (1993).

50. O'Keefe, J. Place units in the hippocampus of the freely moving rat. *Exp. Neurol.* **51**, 78–109 (1976).

51. Wagatsuma, H. & Yamaguchi, Y. Neural dynamics of the cognitive map in the hippocampus. *Cogn. Neurodyn.* **1**, 119–141 (2007).

52. Harvey, C. D., Collman, F., Dombeck, D. A. & Tank, D. W. Intracellular dynamics of hippocampal place cells during virtual navigation. *Nature* **461**, 941–946 (2009).

53. Góis, Z. H. T. D. & Tort, A. B. L. Characterizing Speed Cells in the Rat Hippocampus. *Cell Rep.* **25**, 1872-1884.e4 (2018).

54. Freund, T. F. & Buzsáki, G. Interneurons of the hippocampus. *Hippocampus* **6**, 347–470 (1996).

55. Corrigan, B. W. *et al.* Distinct neural codes in primate hippocampus and lateral prefrontal cortex during associative learning in virtual environments. *Neuron* **110**, 2155-2169.e4 (2022).

56. Sakon, J. J. & Suzuki, W. A. Neural evidence for recognition of naturalistic videos in monkey hippocampus. *Hippocampus* **31**, 916–932 (2021).

57. Robbins, A. A., Fox, S. E., Holmes, G. L., Scott, R. C. & Barry, J. M. Short duration waveforms recorded extracellularly from freely moving rats are representative of axonal activity. *Front. Neural Circuits* **7**, 181 (2013).

58. Wirth, S. *et al.* Single neurons in the monkey hippocampus and learning of new associations. *Science* **300**, 1578–1581 (2003).

59. Skaggs, W. E. *et al.* EEG Sharp Waves and Sparse Ensemble Unit Activity in the Macaque Hippocampus. *J. Neurophysiol.* **98**, 898–910 (2007).

60. Markus, E. J., Barnes, C. A., McNaughton, B. L., Gladden, V. L. & Skaggs, W. E. Spatial information content and reliability of hippocampal CA1 neurons: Effects of visual input. *Hippocampus* **4**, 410–421 (1994).

61. Ravassard, P. *et al.* Multisensory control of hippocampal spatiotemporal selectivity. *Science* **340**, 1342–1346 (2013).

62. Skaggs, W., McNaughton, B. & Gothard, K. An Information-Theoretic Approach to Deciphering the Hippocampal Code. in *Advances in Neural Information Processing Systems* vol. 5 (Morgan-Kaufmann, 1992).

63. O'Keefe, J., Burgess, N., Donnett, J. G., Jeffery, K. J. & Maguire, E. A. Place cells, navigational accuracy, and the human hippocampus. *Philos. Trans. R. Soc. B Biol. Sci.* **353**, 1333–1340 (1998).

64. K, Z., I, G., Bl, M. & Tj, S. Interpreting neuronal population activity by reconstruction: unified framework with application to hippocampal place cells. *J. Neurophysiol.* **79**, (1998).

65. Czurkó, A., Hirase, H., Csicsvari, J. & Buzsáki, G. Sustained activation of hippocampal pyramidal cells by 'space clamping' in a running wheel. *Eur. J. Neurosci.* **11**, 344–352 (1999).

66. Hirase, H., Czurkó, A., Csicsvari, J. & Buzsáki, G. Firing rate and theta-phase coding by hippocampal pyramidal neurons during 'space clamping'. *Eur. J. Neurosci.* **11**, 4373–4380 (1999).

67. Nitz, D. & McNaughton, B. Differential modulation of CA1 and dentate gyrus interneurons during exploration of novel environments. *J. Neurophysiol.* **91**, 863–872 (2004).

68. Maurer, A. P., VanRhoads, S. R., Sutherland, G. R., Lipa, P. & McNaughton, B. L. Self-motion and the origin of differential spatial scaling along the septo-temporal axis of the hippocampus. *Hippocampus* **15**, 841–852 (2005).

69. Kropff, E., Carmichael, J. E., Moser, M.-B. & Moser, E. I. Speed cells in the medial entorhinal cortex. *Nature* **523**, 419–424 (2015).

70. Servén, D. & Brummitt, C. Pygam: Generalized Additive Models In Python. in (Zenodo, 2018). doi:10.5281/ZENODO.1208724.

71. Rigotti, M. *et al.* The importance of mixed selectivity in complex cognitive tasks. *Nature* **497**, 585–590 (2013).

72. Fusi, S., Miller, E. K. & Rigotti, M. Why neurons mix: high dimensionality for higher cognition. *Curr. Opin. Neurobiol.* **37**, 66–74 (2016).

73. Wilson, M. A. & McNaughton, B. L. Dynamics of the Hippocampal Ensemble Code for Space. *Science* **261**, 1055–1058 (1993).

74. Leutgeb, S., Leutgeb, J. K., Treves, A., Moser, M.-B. & Moser, E. I. Distinct Ensemble Codes in Hippocampal Areas CA3 and CA1. *Science* **305**, 1295–1298 (2004).

75. Hazon, O. *et al.* Noise correlations in neural ensemble activity limit the accuracy of hippocampal spatial representations. *Nat. Commun.* **13**, 4276 (2022).

76. Leavitt, M. L., Pieper, F., Sachs, A. J. & Martinez-Trujillo, J. C. Correlated variability modifies working memory fidelity in primate prefrontal neuronal ensembles. *Proc. Natl. Acad. Sci.* **114**, E2494–E2503 (2017).

77. Backen, T., Treue, S. & Martinez-Trujillo, J. C. Encoding of Spatial Attention by Primate Prefrontal Cortex Neuronal Ensembles. *eneuro* **5**, ENEURO.0372-16.2017 (2018).

78. Winson, J. Loss of hippocampal theta rhythm results in spatial memory deficit in the rat. *Science* **201**, 160–163 (1978).

79. Otto, T., Eichenbaum, H., Wible, C. G. & Wiener, S. I. Learning-related patterns of CA1 spike trains parallel stimulation parameters optimal for inducing hippocampal long-term potentiation. *Hippocampus* **1**, 181–192 (1991).

80. Hasselmo, M. E., Bodelón, C. & Wyble, B. P. A proposed function for hippocampal theta rhythm: separate phases of encoding and retrieval enhance reversal of prior learning. *Neural Comput.* **14**, 793–817 (2002).

81. Ekstrom, A. D. *et al.* Human hippocampal theta activity during virtual navigation. *Hippocampus* **15**, 881–889 (2005).

82. Ulanovsky, N. & Moss, C. F. Hippocampal cellular and network activity in freely moving echolocating bats. *Nat. Neurosci.* **10**, 224–233 (2007).

83. Watrous, A. J., Tandon, N., Conner, C. R., Pieters, T. & Ekstrom, A. D. Frequency-specific network connectivity increases underlie accurate spatiotemporal memory retrieval. *Nat. Neurosci.* **16**, 349–356 (2013).

84. Jutras, M. J., Fries, P. & Buffalo, E. A. Oscillatory activity in the monkey hippocampus during visual exploration and memory formation. *Proc. Natl. Acad. Sci.* **110**, 13144–13149 (2013).

85. Sobotka, S. & Ringo, J. L. Saccadic eye movements, even in darkness, generate event-related potentials recorded in medial septum and medial temporal cortex. *Brain Res.* **756**, 168–173 (1997).

86. Tolman, E. C. Cognitive maps in rats and men. *Psychol. Rev.* **55**, 189–208 (1948).

87. Squire, L. R. Memory and the hippocampus: A synthesis from findings with rats, monkeys, and humans. *Psychol. Rev.* **99**, 195–231 (1992).

88. Muller, R. U., Poucet, B., Fenton, A. A. & Cressant, A. Is the hippocampus of the rat part of a specialized navigational system? *Hippocampus* **9**, 413–422 (1999).

89. Preston-Ferrer, P. & Burgalossi, A. Linking neuronal structure to function in rodent hippocampus: a methodological prospective. *Cell Tissue Res.* **373**, 605–618 (2018).

90. Burn, C. C. What is it like to be a rat? Rat sensory perception and its implications for experimental design and rat welfare. *Appl. Anim. Behav. Sci.* **112**, 1–32 (2008).

91. Kaas, J. H., Qi, H.-X. & Stepniewska, I. Escaping the nocturnal bottleneck, and the evolution of the dorsal and ventral streams of visual processing in primates. *Philos. Trans. R. Soc. B Biol. Sci.* **377**, 20210293.

92. Mitchell, J. F. & Leopold, D. A. The marmoset monkey as a model for visual neuroscience. *Neurosci. Res.* **93**, 20–46 (2015).

93. Solomon, S. G. & Rosa, M. G. P. A simpler primate brain: the visual system of the marmoset monkey. *Front. Neural Circuits* **8**, 96 (2014).

94. Ru, M. & Jl, K. The firing of hippocampal place cells predicts the future position of freely moving rats. *J. Neurosci. Off. J. Soc. Neurosci.* **9**, (1989).

95. Yartsev, M. M. & Ulanovsky, N. Representation of three-dimensional space in the hippocampus of flying bats. *Science* **340**, 367–372 (2013).

96. Baraduc, P., Duhamel, J.-R. & Wirth, S. Schema cells in the macaque hippocampus. *Science* **363**, 635–639 (2019).

97. Van Hoesen, G. W. The parahippocampal gyrus: New observations regarding its cortical connections in the monkey. *Trends Neurosci.* **5**, 345–350 (1982).

98. Insausti, R., Amaral, D. G. & Cowan, W. M. The entorhinal cortex of the monkey: II. Cortical afferents. *J. Comp. Neurol.* **264**, 356–395 (1987).

99. Amaral, D. G. & Witter, M. P. The three-dimensional organization of the hippocampal formation: A review of anatomical data. *Neuroscience* **31**, 571–591 (1989).

100. Suzuki, W. A. & Amaral, D. G. Perirhinal and parahippocampal cortices of the macaque monkey: cortical afferents. *J. Comp. Neurol.* **350**, 497–533 (1994).

101. Liu, C. *et al.* A resource for the detailed 3D mapping of white matter pathways in the marmoset brain. *Nat. Neurosci.* **23**, 271–280 (2020).

102. Killian, N. J., Jutras, M. J. & Buffalo, E. A. A map of visual space in the primate entorhinal cortex. *Nature* **491**, 761–764 (2012).

103. Spalla, D., Treves, A. & Boccara, C. N. Angular and linear speed cells in the parahippocampal circuits. *Nat. Commun.* **13**, 1907 (2022).

104. Keshavarzi, S. *et al.* Multisensory coding of angular head velocity in the retrosplenial cortex. *Neuron* **110**, 532-543.e9 (2022).

105. Bassett, J. P. & Taube, J. S. Neural correlates for angular head velocity in the rat dorsal tegmental nucleus. *J. Neurosci. Off. J. Soc. Neurosci.* **21**, 5740–5751 (2001).

106. Chen, L. L., Lin, L. H., Green, E. J., Barnes, C. A. & McNaughton, B. L. Head-direction cells in the rat posterior cortex. I. Anatomical distribution and behavioral modulation. *Exp. Brain Res.* **101**, 8–23 (1994).

107. Fuhs, M. C. & Touretzky, D. S. A spin glass model of path integration in rat medial entorhinal cortex. *J. Neurosci. Off. J. Soc. Neurosci.* **26**, 4266–4276 (2006).

108. Burgess, N. Grid cells and theta as oscillatory interference: theory and predictions. *Hippocampus* **18**, 1157–1174 (2008).

109. Mcnaughton, B. L., Leonard, B. & Chen, L. Cortical-hippocampal interactions and cognitive mapping: A hypothesis based on reintegration of the parietal and inferotemporal pathways for visual processing. *Psychobiology* **17**, 230–235 (1989).

110. Campbell, M. G. *et al.* Principles governing the integration of landmark and self-motion cues in entorhinal cortical codes for navigation. *Nat. Neurosci.* **21**, 1096–1106 (2018).

111. Johnston, W. J., Palmer, S. E. & Freedman, D. J. Nonlinear mixed selectivity supports reliable neural computation. *PLOS Comput. Biol.* **16**, e1007544 (2020).

112. Cushman, J. D. *et al.* Multisensory Control of Multimodal Behavior: Do the Legs Know What the Tongue Is Doing? *PLoS ONE* **8**, e80465 (2013).

113. Acharya, L., Aghajan, Z. M., Vuong, C., Moore, J. J. & Mehta, M. R. Causal Influence of Visual Cues on Hippocampal Directional Selectivity. *Cell* **164**, 197–207 (2016).

114. Purandare, C. S. *et al.* Moving bar of light evokes vectorial spatial selectivity in the immobile rat hippocampus. *Nature* **602**, 461–467 (2022).

115. Jercog, P. E. *et al.* Heading direction with respect to a reference point modulates place-cell activity. *Nat. Commun.* **10**, 2333 (2019).

116. Wood, E. R., Dudchenko, P. A. & Eichenbaum, H. The global record of memory in hippocampal neuronal activity. *Nature* **397**, 613–616 (1999).

117. Burgess, N. *Spatial Cognition and the Brain*. *Ann. N. Y. Acad. Sci.* **1124**, 77–97 (2008).

118. Buzsáki, G. Two-stage model of memory trace formation: a role for ‘noisy’ brain states. *Neuroscience* **31**, 551–570 (1989).

119. Battaglia, F. P., Benchenane, K., Sirota, A., Pennartz, C. M. A. & Wiener, S. I. The hippocampus: hub of brain network communication for memory. *Trends Cogn. Sci.* **15**, 310–318 (2011).

120. Buzsáki, G. Theta oscillations in the hippocampus. *Neuron* **33**, 325–340 (2002).

121. Jacobs, J. Hippocampal theta oscillations are slower in humans than in rodents: implications for models of spatial navigation and memory. *Philos. Trans. R. Soc. Lond. B. Biol. Sci.* **369**, 20130304 (2014).

122. Goyal, A. *et al.* Functionally distinct high and low theta oscillations in the human hippocampus. *Nat. Commun.* **11**, 2469 (2020).

123. Schroeder, C. E., Lakatos, P., Kajikawa, Y., Partan, S. & Puce, A. Neuronal oscillations and visual amplification of speech. *Trends Cogn. Sci.* **12**, 106–113 (2008).

124. Macrides, F., Eichenbaum, H. B. & Forbes, W. B. Temporal relationship between sniffing and the limbic theta rhythm during odor discrimination reversal learning. *J. Neurosci. Off. J. Soc. Neurosci.* **2**, 1705–1717 (1982).

125. Martinez-Trujillo, J. Corollary discharge: Linking saccades and memory circuits in the human brain. *Curr. Biol. CB* **32**, R774–R776 (2022).

126. Katz, C. N. *et al.* A corollary discharge mediates saccade-related inhibition of single units in mnemonic structures of the human brain. *Curr. Biol.* **32**, 3082-3094.e4 (2022).

127. Sun, L. D. & Goldberg, M. E. Corollary Discharge and Oculomotor Proprioception: Cortical Mechanisms for Spatially Accurate Vision. *Annu. Rev. Vis. Sci.* **2**, 61–84 (2016).

128. Rao, H. M., Mayo, J. P. & Sommer, M. A. Circuits for presaccadic visual remapping. *J. Neurophysiol.* **116**, 2624–2636 (2016).

129. Sommer, M. A. & Wurtz, R. H. Brain circuits for the internal monitoring of movements. *Annu. Rev. Neurosci.* **31**, 317 (2008).

130. Berman, R. A., Cavanaugh, J., McAlonan, K. & Wurtz, R. H. A circuit for saccadic suppression in the primate brain. *J. Neurophysiol.* **117**, 1720–1735 (2017).

131. Hwang, J., Mitz, A. R. & Murray, E. A. NIMH MonkeyLogic: Behavioral control and data acquisition in MATLAB. *J. Neurosci. Methods* **323**, 13–21 (2019).

132. Kikinis, R., Pieper, S. D. & Vosburgh, K. G. 3D Slicer: A Platform for Subject-Specific Image Analysis, Visualization, and Clinical Support. in *Intraoperative Imaging and Image-Guided Therapy* (ed. Jolesz, F. A.) 277–289 (Springer, 2014). doi:10.1007/978-1-4614-7657-3_19.

133. Kapur, T. *et al.* Increasing the impact of medical image computing using community-based open-access hackathons: The NA-MIC and 3D Slicer experience. *Med. Image Anal.* **33**, 176–180 (2016).

134. Fedorov, A. *et al.* 3D Slicer as an Image Computing Platform for the Quantitative Imaging Network. *Magn. Reson. Imaging* **30**, 1323–1341 (2012).

135. Franzius, M., Sprekeler, H. & Wiskott, L. Slowness and Sparseness Lead to Place, Head-Direction, and Spatial-View Cells. *PLOS Comput. Biol.* **3**, e166 (2007).

136. Ranck, J. B. Studies on single neurons in dorsal hippocampal formation and septum in unrestrained rats. I. Behavioral correlates and firing repertoires. *Exp. Neurol.* **41**, 461–531 (1973).

137. Royer, S. *et al.* Control of timing, rate and bursts of hippocampal place cells by dendritic and somatic inhibition. *Nat. Neurosci.* **15**, 769–775 (2012).

138. Buckmaster, P. S. & Amaral, D. G. Intracellular recording and labeling of mossy cells and proximal CA3 pyramidal cells in macaque monkeys. *J. Comp. Neurol.* **430**, 264–281 (2001).

139. Xu, J. & Clancy, C. E. Ionic Mechanisms of Endogenous Bursting in CA3 Hippocampal Pyramidal Neurons: A Model Study. *PLoS ONE* **3**, e2056 (2008).

140. Livingstone, M. S., Freeman, D. C. & Hubel, D. H. Visual responses in V1 of freely viewing monkeys. *Cold Spring Harb. Symp. Quant. Biol.* **61**, 27–37 (1996).

141. Hastie, T. J. & Tibshirani, R. J. *Generalized Additive Models*. (CRC Press, 1990).

142. Wood, S. N. *Generalized Additive Models: An Introduction with R, Second Edition*. (Chapman and Hall/CRC, 2017). doi:10.1201/9781315370279.

143. Oostenveld, R., Fries, P., Maris, E. & Schoffelen, J.-M. FieldTrip: Open Source Software for Advanced Analysis of MEG, EEG, and Invasive Electrophysiological Data. *Comput. Intell. Neurosci.* **2011**, e156869 (2010).

144. Donoghue, T. *et al.* Parameterizing neural power spectra into periodic and aperiodic components. *Nat. Neurosci.* **23**, 1655–1665 (2020).

Supplementary Material:

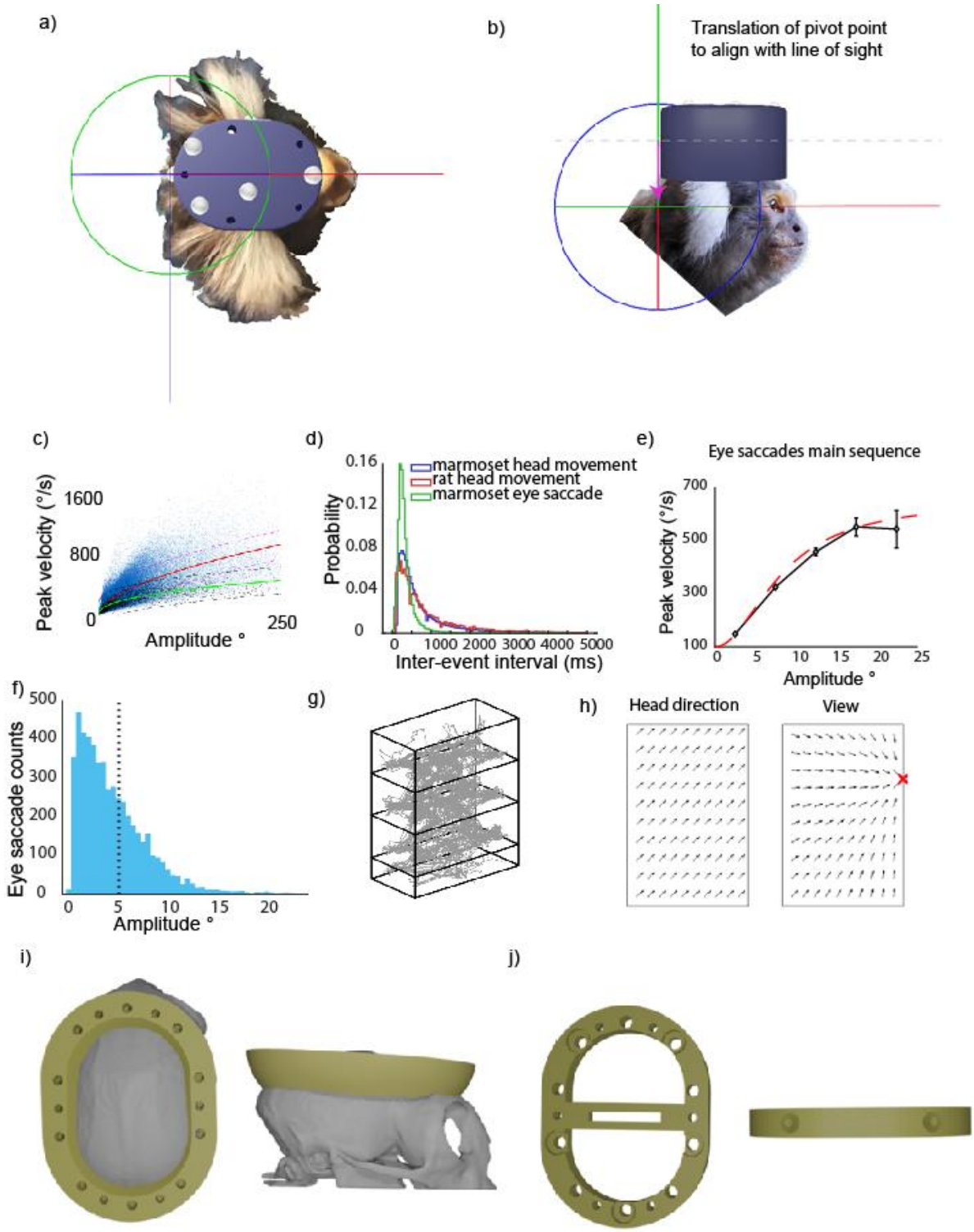

Supplementary figure 1 (a) View from the top showing the alignment of the roll axis (red) with the visual axis, assuming a cyclopean eye. **(b)** Diagram illustrating the position of the pivot point (origin of rotation angles). The position of the pivot point (originally placed in the position of the most posterior retro-reflective marker) is linearly translated downwards, along the vertical axis to align with the subject's visual axis. **(c)** Main sequence (amplitude vs peak velocity) of head movements and Naka-Rushton function fit, for marmoset (blue markers, red line) and rat (black markers, green line); dashed lines correspond to 95% confidence intervals. **(d)** Distribution of inter-event interval for marmoset and rat head movements (blue and red distributions respectively) and marmoset eye saccades (green distribution). **(e)** Main sequence (amplitude vs peak velocity) of marmoset eye saccades, error bars convey 95% confidence intervals. The dashed line corresponds to a Naka-Rushton function fit. **(f)** Distribution of marmoset eye saccade amplitudes, dashed line placed at 5°. **(g)** Example trajectory traces (gray) of the 3D position during a recording session for subject C. **(h)** Illustration taken from a previous publication[135], displays the vector direction differences between head direction and view encoding. **(i)** 3D model of the recording chamber ring placed on the skull of the marmoset. **(j)** 3D model of the spacer that houses the electrode connector (omnentics 36pin), the spacer is placed on top of the chamber ring and it serves as a head-fixation base.

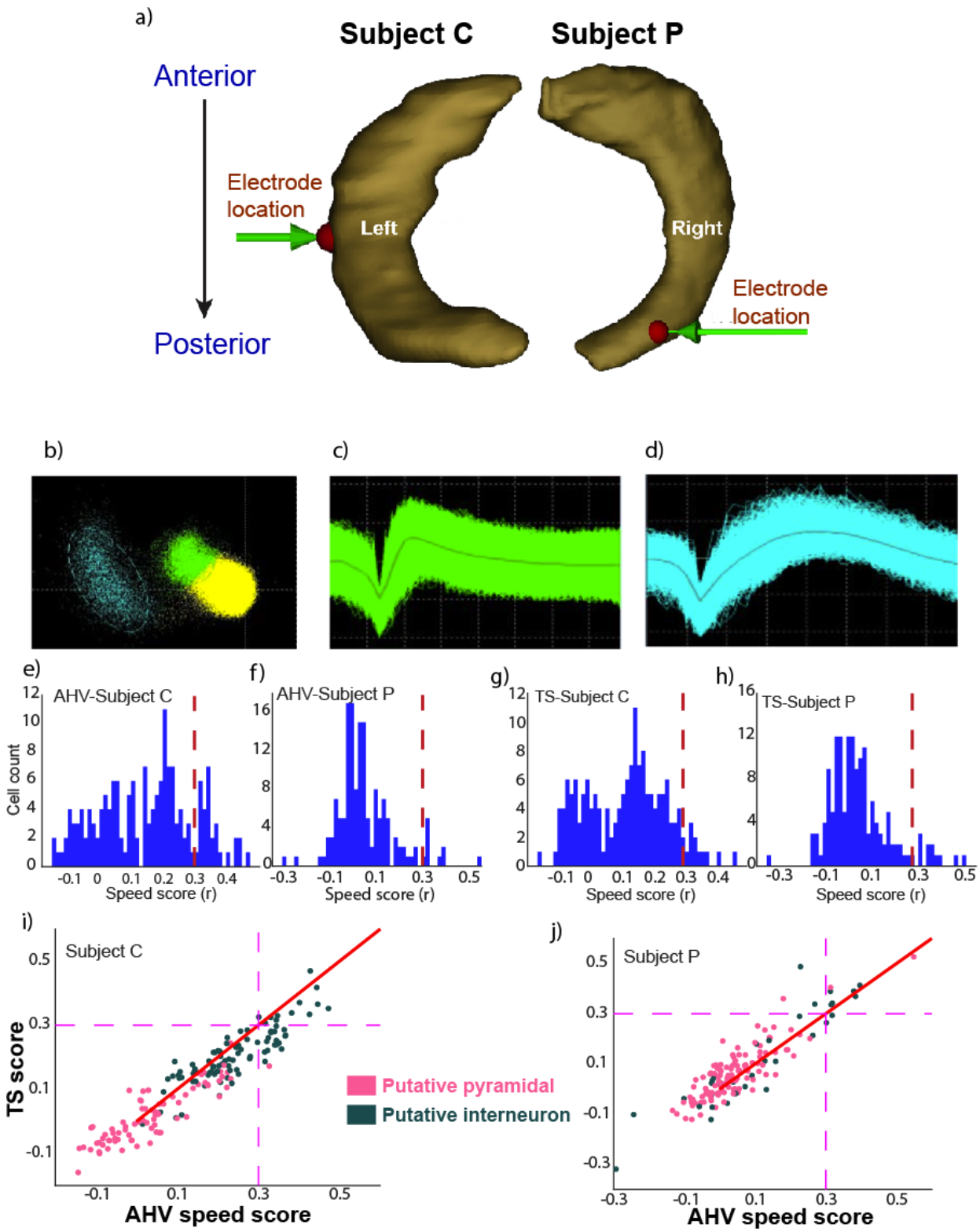
a)
Subject C
Subject P
Anterior
Posterior
Electrode location
Left
Right
Electrode location
b)
c)
d)
e)
AHV-Subject C
Cell count
Speed score (r)
f)
AHV-Subject P
Speed score (r)
g)
TS-Subject C
Speed score (r)
h)
TS-Subject P
Speed score (r)
i)
Subject C
TS score
AHV speed score
Putative pyramidal
Putative interneuron
j)
Subject P
AHV speed score

Supplementary figure 2 (a) MRI and micro-CT based 3D reconstruction of the electrode recording sites for subject C (left hippocampus) and subject P (right hippocampus). **(b)** Screenshot of a sorting session of one channel using Plexon software (Offline Sorter, Plexon Inc., Texas, USA). PCA view is displayed with labelled clusters, blue is a single unit, green is multi-unit activity, and yellow is the noise unit. **(c)** Multi-unit activity spike waveforms, aligned to the negative peak. **(d)** Single unit activity spike waveforms, aligned to the negative peak. **(e,f)** AHV speed scores for subject C and subject P respectively, the dashed line indicates a speed score of 0.3. **(g,h)** TS speed scores for subject C and subject P respectively, the dashed line indicates a speed score of 0.3. **(i,j)** Speed score distribution for both AHV and TS labelled according to cell type for subject C and subject P respectively, (green = putative interneuron, pink = putative pyramidal), the dashed line indicates a speed score of 0.3.

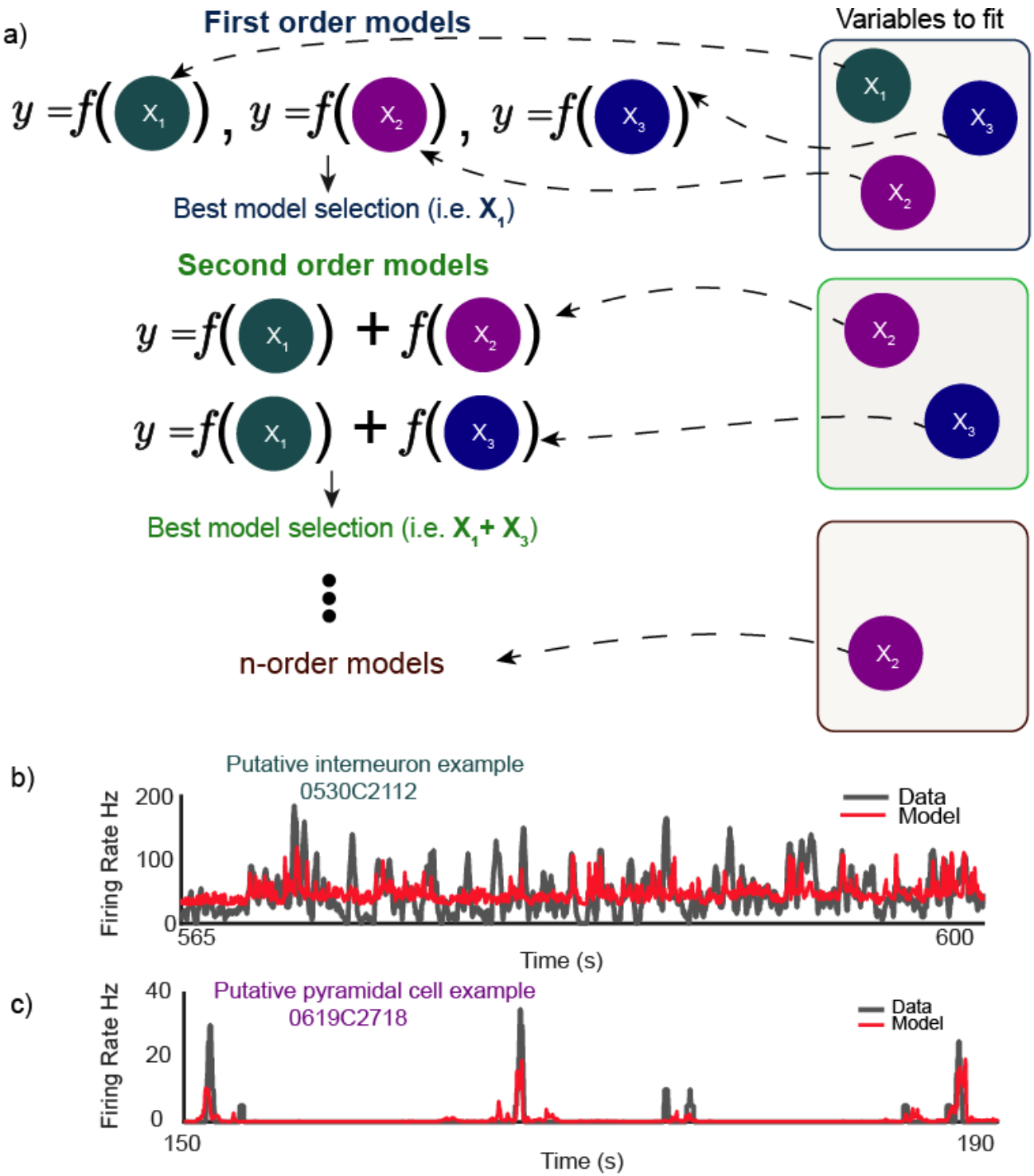

Supplementary figure 3 (a) Schematic describing the stepwise forward search GAM model selection process. **(b)** Real vs. predicted firing rate for a putative interneuron example cell (example cell from **Fig.6c**). **(c)** Real vs. predicted firing rate for a putative pyramidal example cell (example cell from **Fig.6a**).

First order model encoding cells:

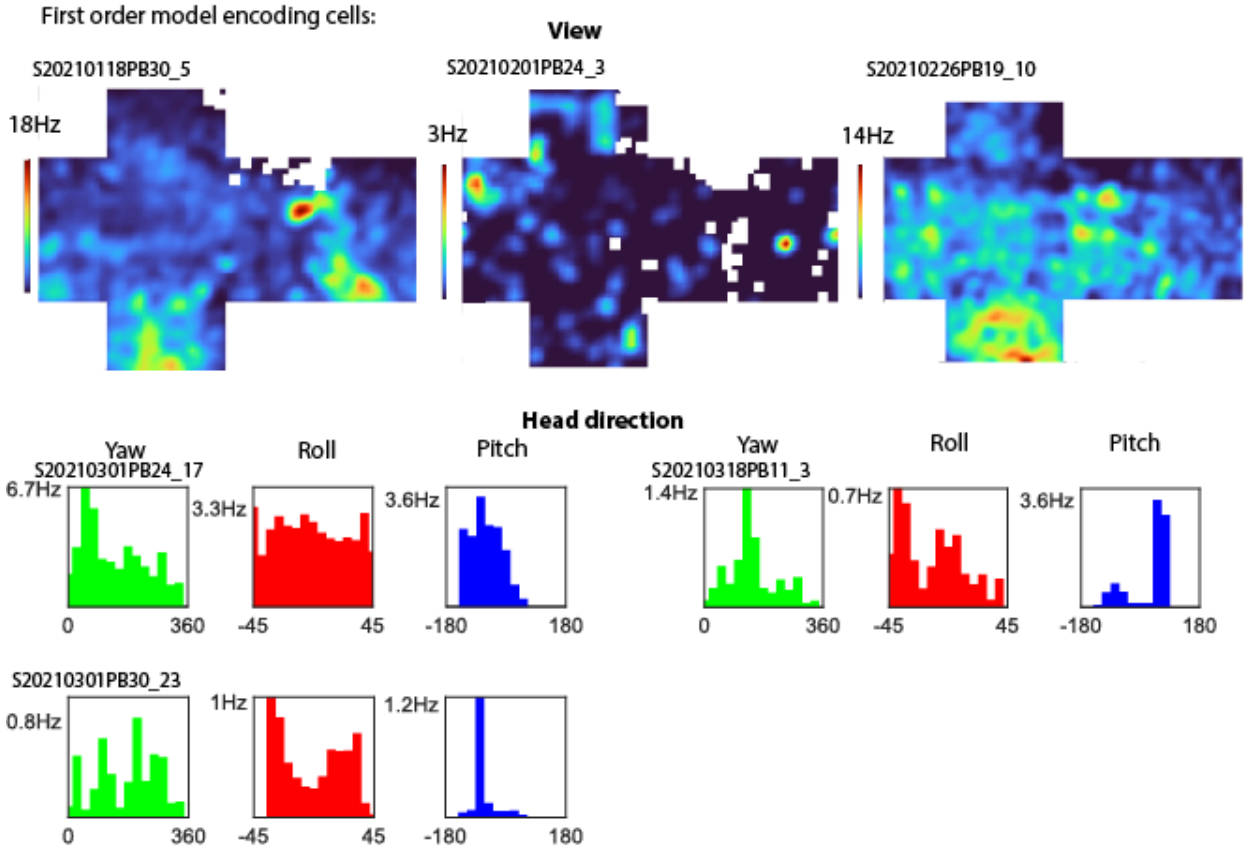

Second order model encoding cells:

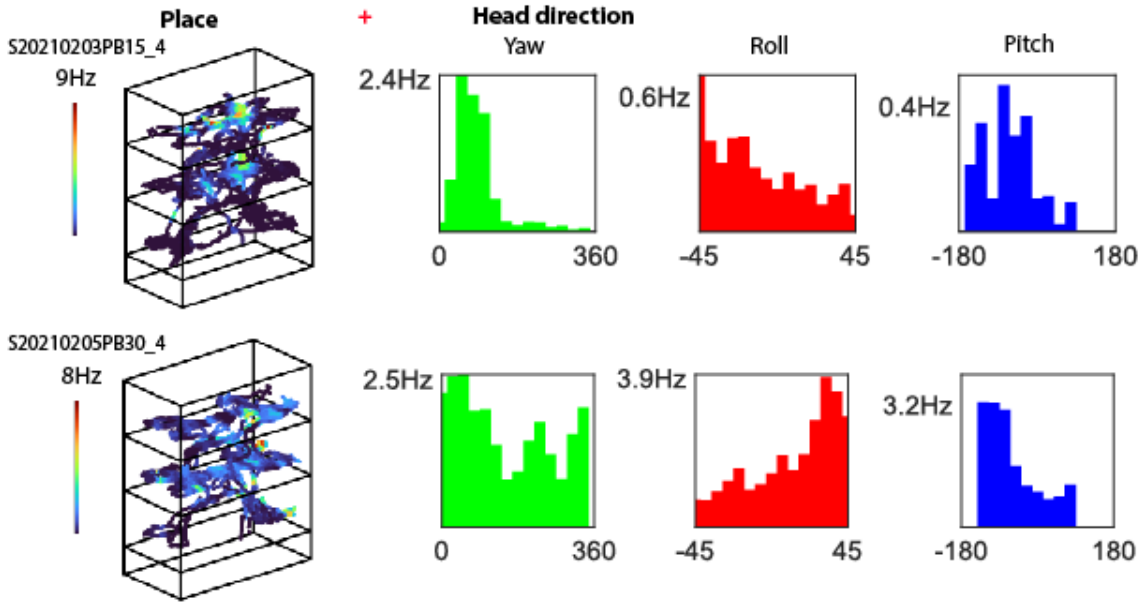

Second order model encoding cells:

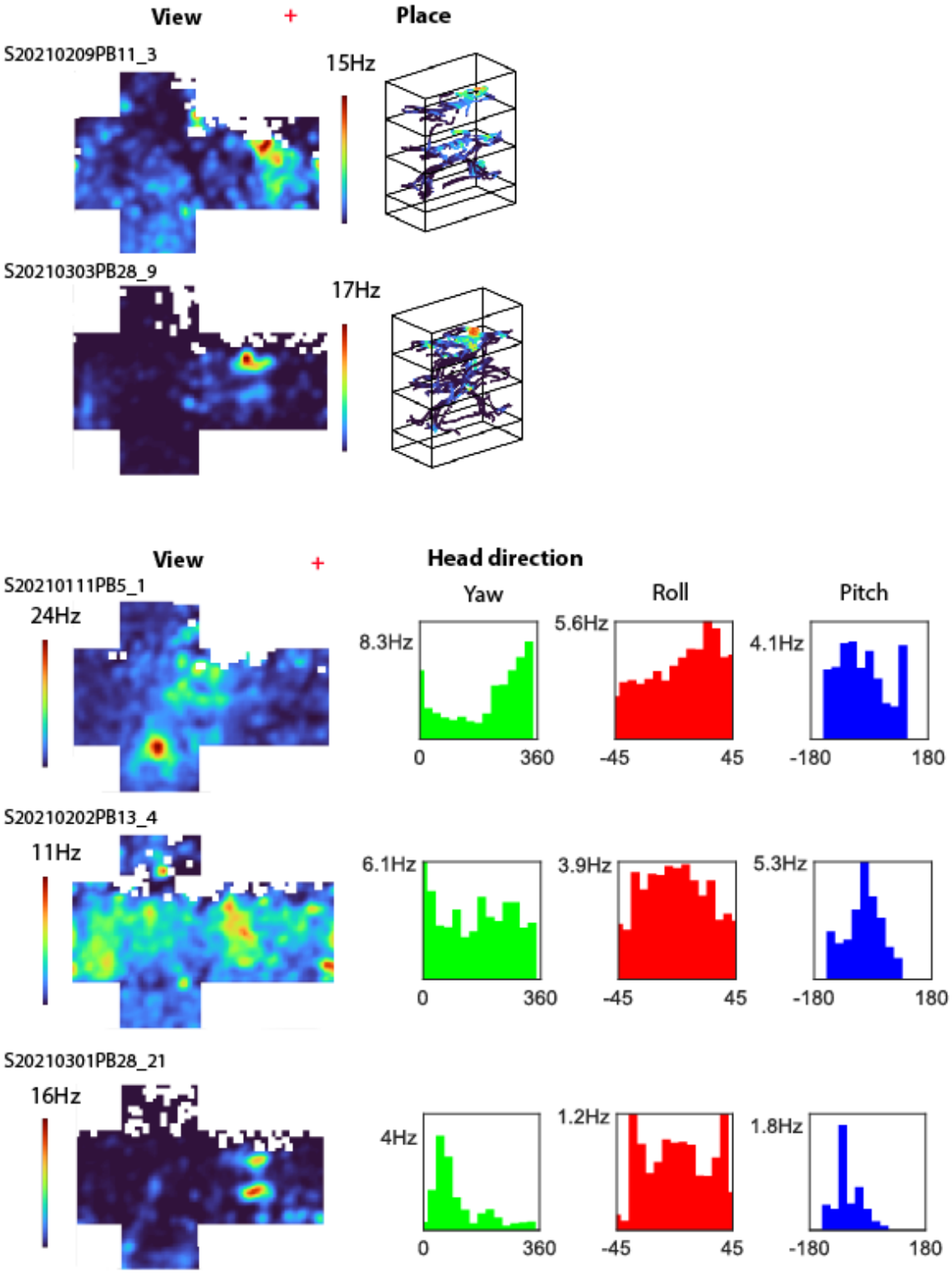

Third order model encoding cells:

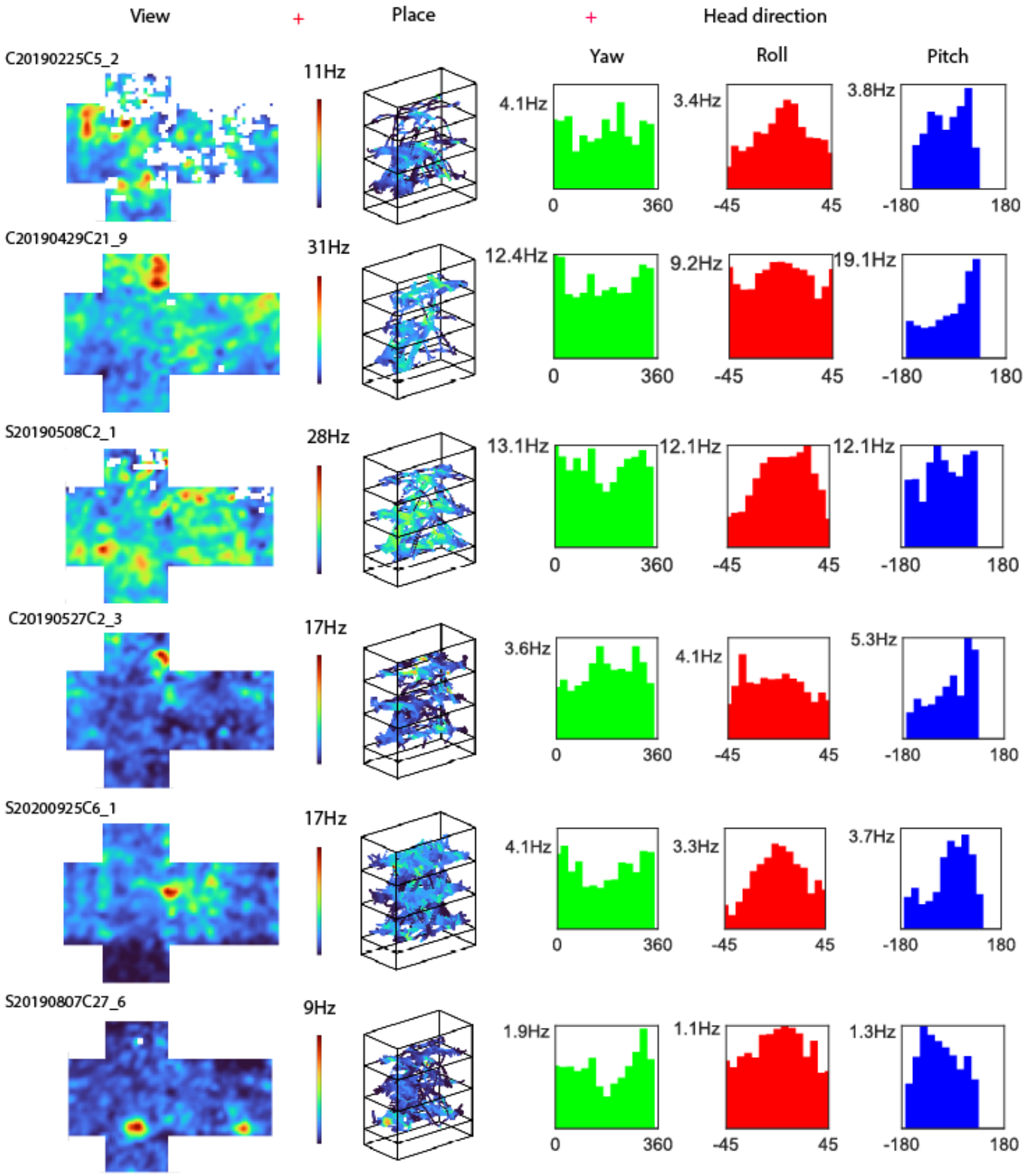

Third order model encoding cells:

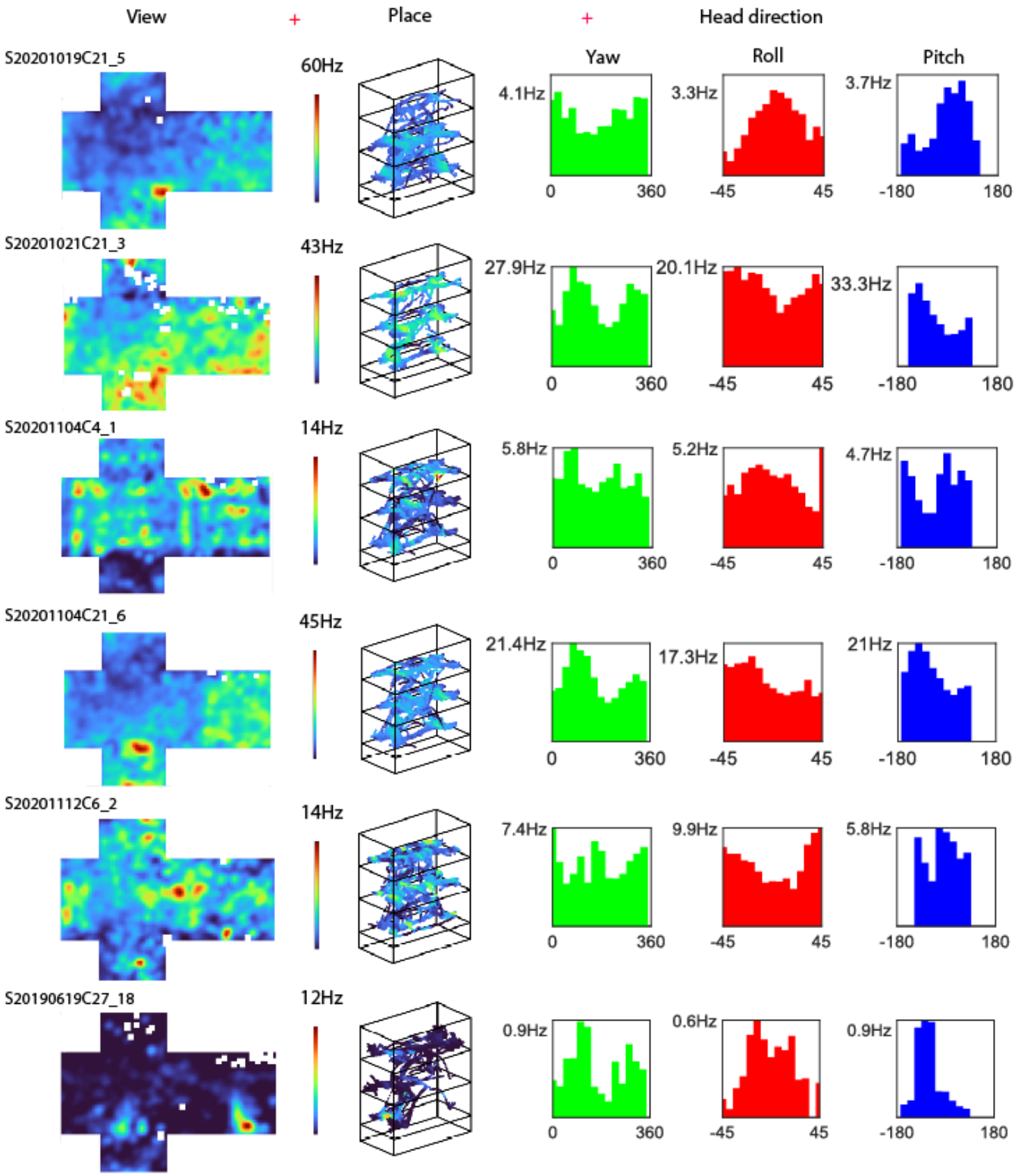

Third order model encoding cells:

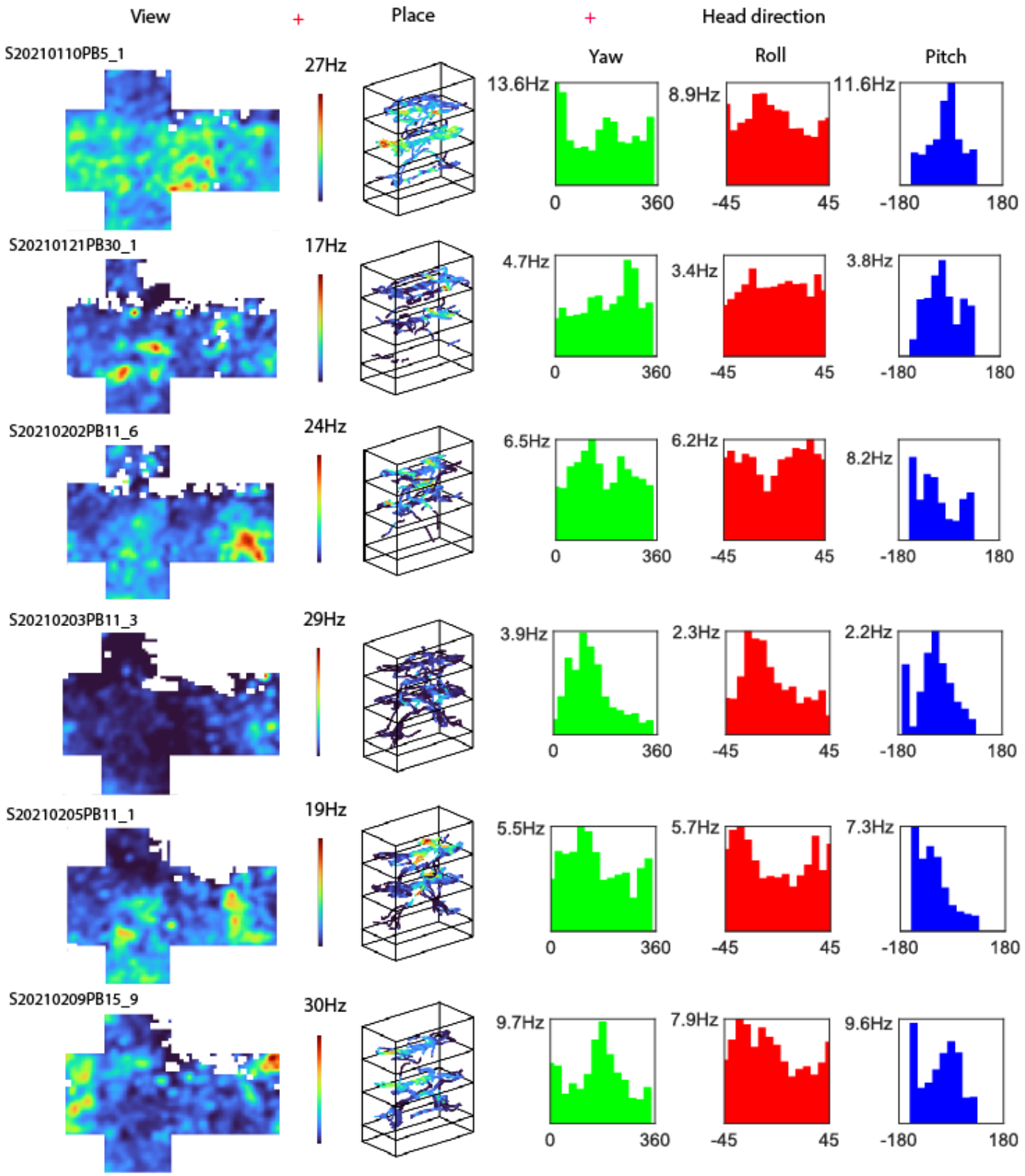

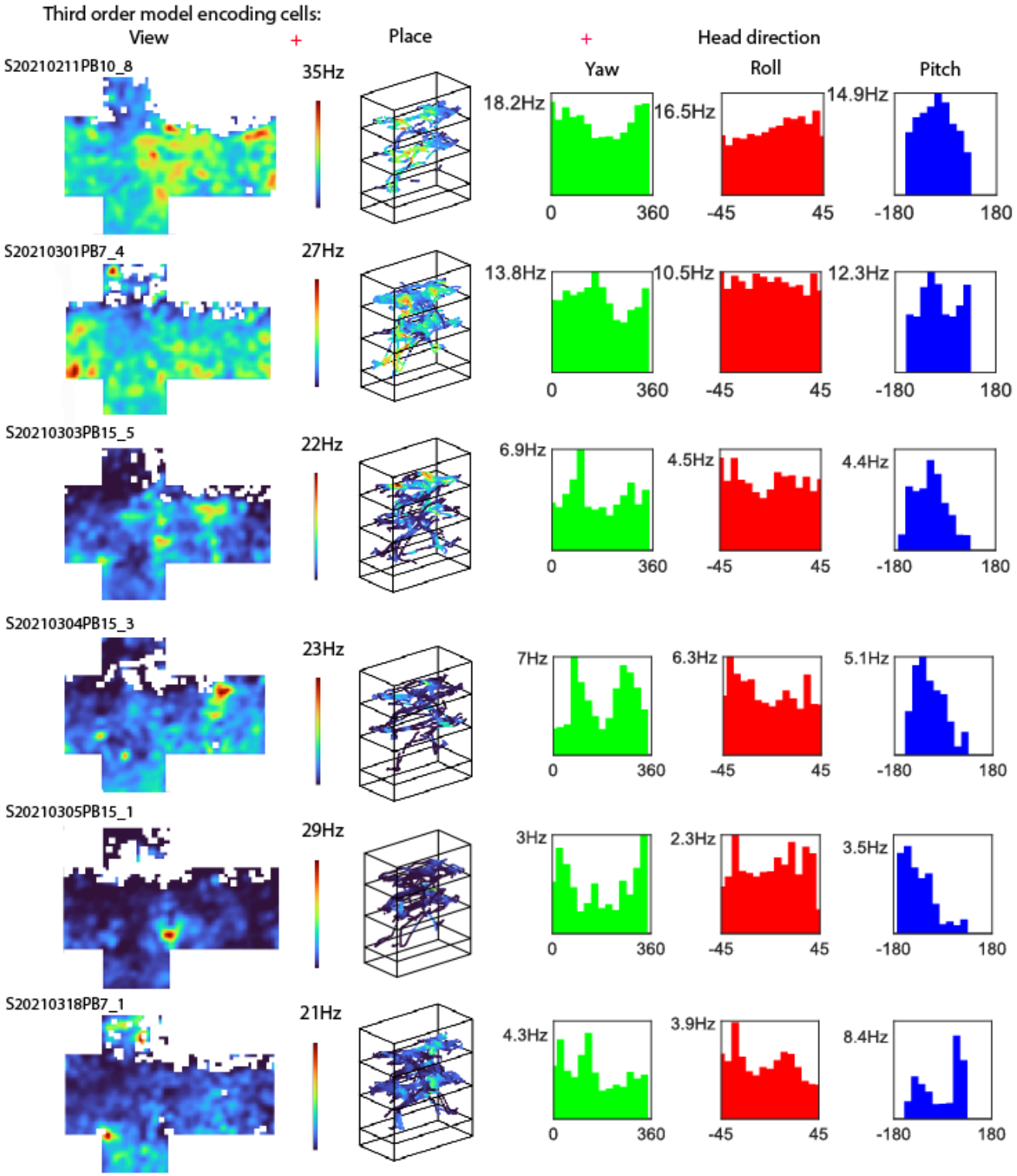
Third order model encoding cells:
View
+
Place
+
Head direction
Yaw
Roll
Pitch
S20210211PB10_8
35Hz
18.2Hz
16.5Hz
14.9Hz
0
360
-45
45
-180
180
S20210301PB7_4
27Hz
13.8Hz
10.5Hz
12.3Hz
0
360
-45
45
-180
180
S20210303PB15_5
22Hz
6.9Hz
4.5Hz
4.4Hz
0
360
-45
45
-180
180
S20210304PB15_3
23Hz
7Hz
6.3Hz
5.1Hz
0
360
-45
45
-180
180
S20210305PB15_1
29Hz
3Hz
2.3Hz
3.5Hz
0
360
-45
45
-180
180
S20210318PB7_1
21Hz
4.3Hz
3.9Hz
8.4Hz
0
360
-45
45
-180
180

Supplementary figure 4 Additional single-cell examples are provided to illustrate the diverse types of encoding observed in putative pyramidal single neurons using the GAM model. Rate maps depicting view, place, and head direction are plotted to represent the corresponding behaviors encoded by individual neurons. In the case of cells encoding only one variable (first order models), a single rate map is observed. Conversely, in cells encoding multiple variables (second and third order models) multiple rate maps are displayed, indicating the specific behaviors being encoded. In head direction rate maps, firing rates corresponding to yaw angles (horizontal head direction) are color-coded as green, roll angles (lateral tilt) as red, and pitch angles (vertical axis) as blue. In the case of third order models, the view and place rate maps share the same color map, with the maximum firing rate indicated at the top of the color bar.

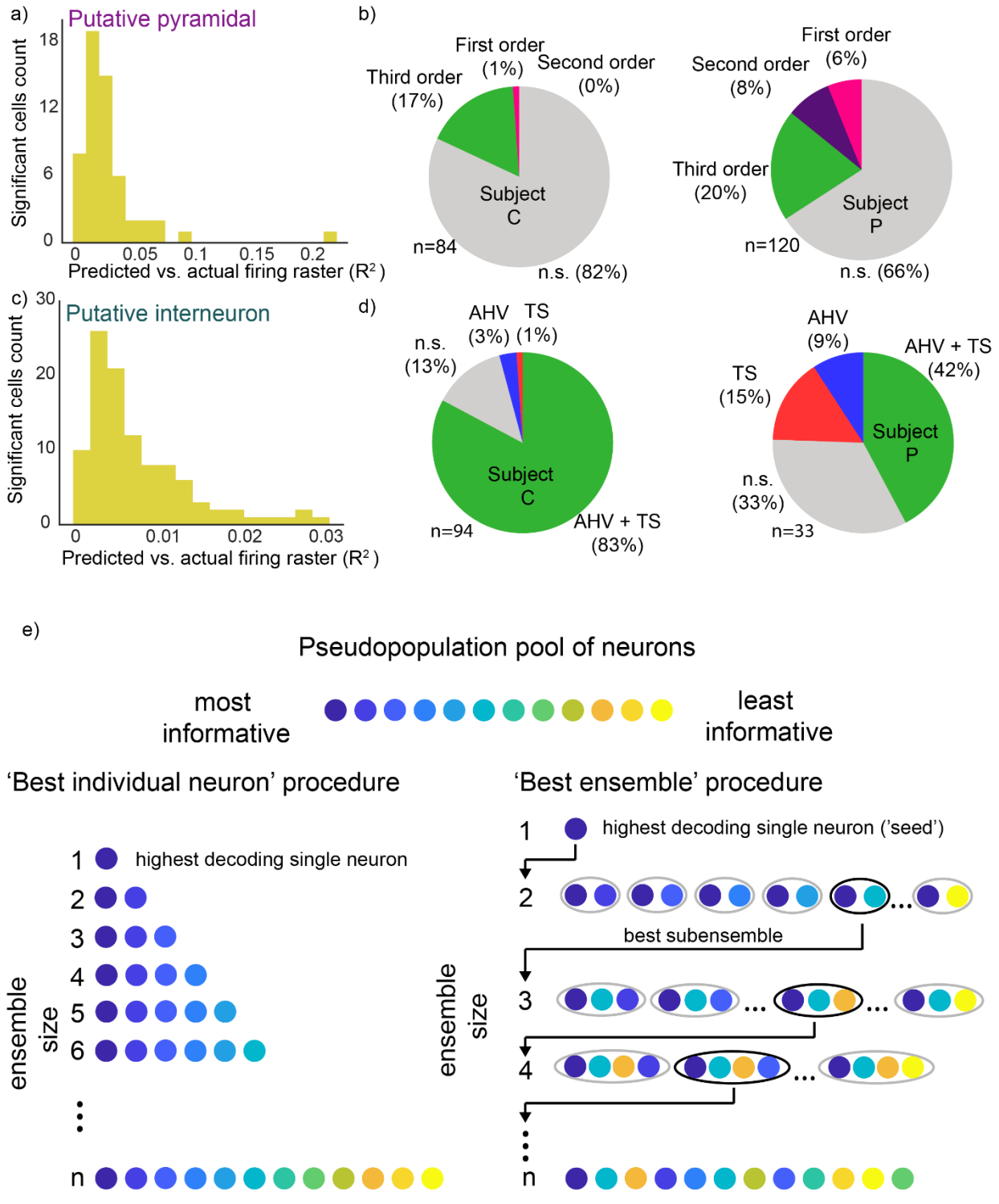
a)
Putative pyramidal
Significant cells count
18
12
6
0
0
0.05
0.1
0.15
0.2
Predicted vs. actual firing raster (R²)
b)
First order (1%)
Second order (0%)
Third order (17%)
Subject C
n=84
n.s. (82%)
First order (6%)
Second order (8%)
Third order (20%)
Subject P
n=120
n.s. (66%)
c)
Putative interneuron
Significant cells count
30
20
10
0
0
0.01
0.02
0.03
Predicted vs. actual firing raster (R²)
d)
AHV (3%)
TS (1%)
n.s. (13%)
Subject C
n=94
AHV + TS (83%)
AHV (9%)
AHV + TS (42%)
TS (15%)
Subject P
n.s. (33%)
n=33
e)
Pseudopopulation pool of neurons
most informative
least informative
'Best individual neuron' procedure
highest decoding single neuron
ensemble size
1
2
3
4
5
6
n
'Best ensemble' procedure
highest decoding single neuron ('seed')
best subensemble
ensemble size
1
2
3
4
n

Supplementary figure 5 (a) Average R^2 between predicted and real spike rasters of all significantly encoding putative pyramidal cells. **(b)** Proportion of putative pyramidal encoding cells for subject C (left) and subject P (right). **(c)** Average R^2 between predicted and real spike rasters of all significantly encoding putative interneuron cells. **(d)** Proportion of putative interneuron encoding cells for subject C (left) and subject P (right). Since each recording session is divided into 5 equally-timed folds, each predicted raster is a continuous time series approximately 8-12 min. long. **(e)** Schematic describing the best ensemble building procedure. (left) The most informative neuron is selected, as assessed by the single-neuron with the highest SVM decoding accuracy of place. (right) The most informative neuron is used as a seed to iteratively add units (looped through the remaining units) to the subsequent subensembles until the 'best ensemble' n-combination of neurons is obtained.

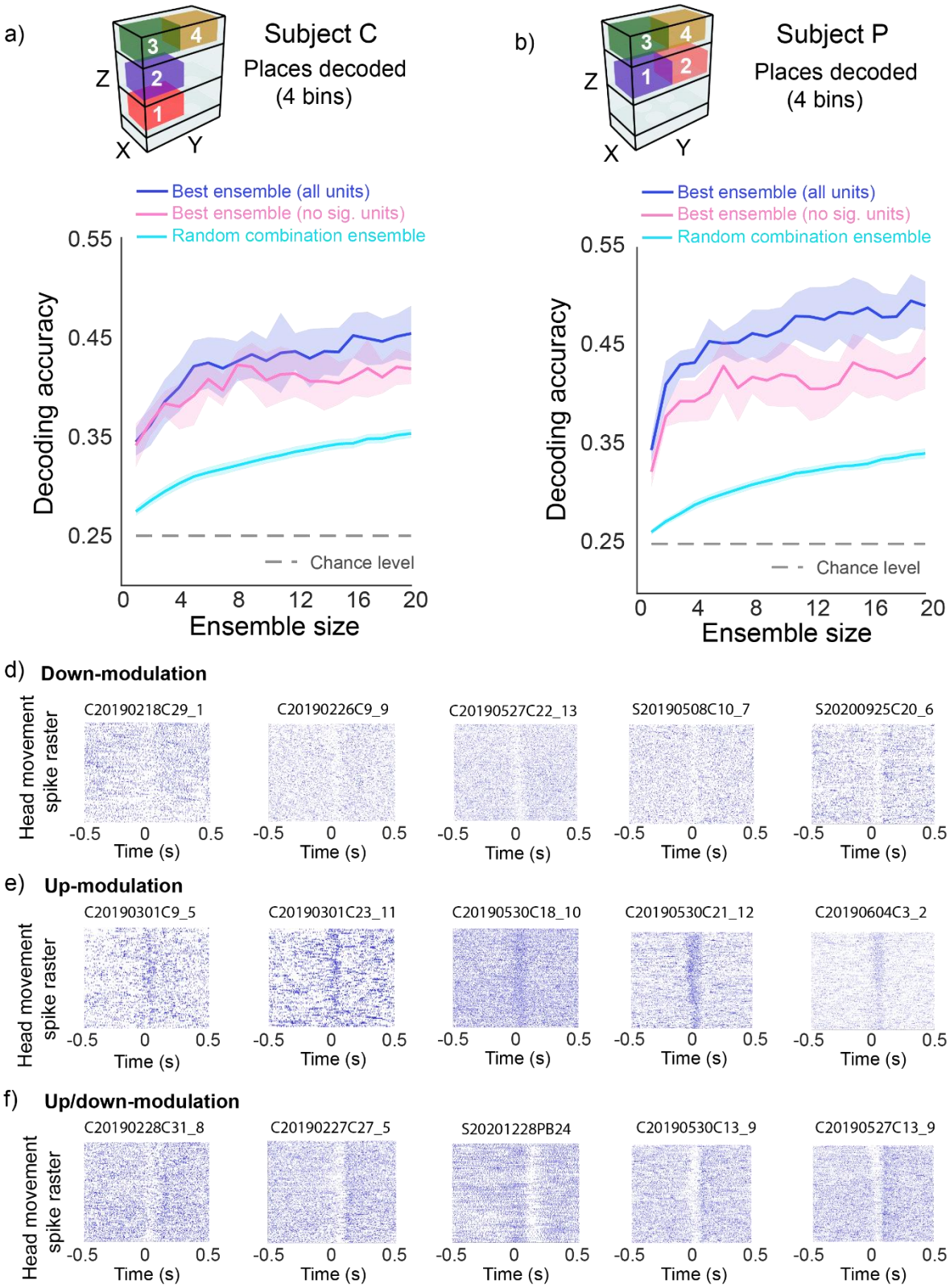
a)
Subject C
Places decoded
(4 bins)
Z
X
Y
1
2
3
4
b)
Subject P
Places decoded
(4 bins)
Best ensemble (all units)
Best ensemble (no sig. units)
Random combination ensemble
Decoding accuracy
0.55
0.45
0.35
0.25
Chance level
0
4
8
12
16
20
Ensemble size
d) Down-modulation
e) Up-modulation
f) Up/down-modulation
Head movement
spike raster
C20190218C29_1
C20190226C9_9
C20190527C22_13
S20190508C10_7
S20200925C20_6
C20190301C9_5
C20190301C23_11
C20190530C18_10
C20190530C21_12
C20190604C3_2
C20190228C31_8
C20190227C27_5
S20201228PB24
C20190530C13_9
C20190527C13_9
-0.5
0
0.5
Time (s)

Supplementary figure 6 (a,b) (top) 3D diagram of the binned place locations used to decode the subject's position, (bottom) blue and pink lines correspond to raw decoding accuracy (y axis) as a function ensemble size (number of neurons, x axis), shaded area corresponds to 95% confidence intervals. Blue solid lines correspond to the best ensemble constructed from a pool of all recorded putative pyramidal neurons. Pink solid lines correspond to the best ensemble constructed from a pool of non significantly selective cells (as per GAM encoding analysis). R^2 goodness of fit value is reported. The cyan lines correspond to decoding accuracy of a randomized combination of neurons (100 iterations), shaded area corresponds to 95% confidence intervals. The gray dashed lines correspond to chance decoding accuracy (1/4, 0.25). **(d,e,f)** Additional single-cell examples of down-modulated, up-modulated and up/down modulated cells respectively. Each raster plot corresponds to a single neuron and is aligned (time 0) with the peak velocity time of a head movement, where each row corresponds to one head movement event and each blue dot represents one neuronal spike, negative times indicate the neuron's firing before the peak velocity of a head movement, while positive times indicate the neuron's firing afterwards.

Supplementary movie 1: **https://youtu.be/Vz4lMer5g8o** (Recording session video example)